The Sugar-to-Flower Shallow Cumulus Transition Under the Influences of Diurnal Cycle and Free-Tropospheric Mineral Dust

Pornampai Narenpitak[1,2,3], Jan Kazil[1,2], Takanobu Yamaguchi[1,2], Patricia K. Quinn[4], Graham Feingold[2]

[1]Cooperative Institute for Research in Environmental Sciences,
University of Colorado Boulder, Boulder, Colorado, USA
[2]National Oceanic and Atmospheric Administration,
Chemical Sciences Laboratory, Boulder, Colorado, USA
[3]Data-driven Simulation and Systems Research Team,
National Electronics and Computer Technology Center, Pathum Thani, Thailand
[4]National Oceanic and Atmospheric Administration,
Pacific Marine Environmental Laboratory, Seattle, Washington, USA

Key Points:

- The transition from sugar to flowers occurs more rapidly at night, producing more cloud and rain, with stronger organization and cold pools
- Precipitation and cold pools counteract the mechanism of cloud aggregation, transporting moisture to drier regions to form new convection
- Mineral dust above the clouds modulates radiative fluxes below, strengthening mesoscale circulation and cloud organization during the day

Corresponding author: Pornampai Narenpitak, pornampai.nar@nectec.or.th

Abstract

A transition from sugar to flower shallow cumuli occurred under a layer of mineral dust on February 2, 2020, during the multinational ATOMIC and EUREC^{4}A campaign. Lagrangian large eddy simulations following an airmass trajectory along the trade winds are used to explore radiative impacts of the diurnal cycle and mineral dust on the sugar-to-flower (S2F) cloud transition. The large-scale meteorological forcing is derived from the European Center for Medium-Range Weather Forecasts Reanalysis 5^{th} Generation and based on in-situ measurements during the field campaign. A 12-hour delay in the diurnal cycle accelerates the S2F transition, leading to more cloud liquid water and precipitation at night. The aggregated clouds generate more, and stronger cold pools, which alter the original mechanism responsible for the organization. Although there is still mesoscale moisture convergence in the cloud layer, the near-surface divergence associated with cold pools transports the subcloud moisture to the drier surrounding regions. New convection forms along the cold pool edges, resulting in the next generation of flower clouds. The amount of cloud water, rain, and cold pools reduce after sunrise. The modulation of the surface radiative budget by free-tropospheric mineral dust poses a less dramatic effect on the S2F transition. Mineral dust absorbs shortwave radiation during the day, cooling the boundary layer temperature, enabling stronger turbulence, strengthening the mesoscale organization, and enlarging the aggregate areas. At night, the longwave heating effects of the mineral dust and more cloud liquid water warms the boundary layer, reducing the cloud amount and weakening the organization.

Plain Language Summary

During a joint field study called ATOMIC and EUREC^{4}A, a transition between two cloud systems took place during the day on February 2, 2020. Very small and shallow clouds called "sugar" transitioned into deeper and wider cloud aggregates called "flowers." A dense mineral dust layer was also observed above the trade-wind cumulus cloud field, likely modulating the radiation interacting with the clouds. High-resolution simulations are applied to help understand the same cloud transition if it had taken place at night, and to explore the impacts of mineral dust on the transition. A 12-hour delay in the daily cycle affects the cloud transition much more significantly, resulting in more clouds and rain at night. The mineral dust blocks the solar radiation and cools the air beneath during the day, but does not change the cloud and rain amount as much.

1 Introduction

Trade-wind shallow cumulus plays an important role in Earth's radiation budget. These clouds are ubiquitous over tropical and subtropical oceans and reflect solar radiation, reducing the planetary albedo and cooling the boundary layer. The low-level clouds are a leading source of climate uncertainty in global climate models (e.g., Bony & Dufresne, 2005; Medeiros et al., 2008; Andrews et al., 2012; Boucher et al., 2013; Zelinka et al., 2016, 2020, and others). The uncertainty arises from challenges in representing the cloud liquid water, cloud structure, spatial patterns, precipitation and other internal processes that modulate the radiative properties of the clouds (Stevens et al., 2001; Xu et al., 2010; Rieck et al., 2012; Zhang et al., 2013; Bretherton et al., 2013; Blossey et al., 2013; Nuijens & Siebesma, 2019). In addition, shallow cumulus clouds are also sensitive to humidity and temperature of the boundary layer, which can be modulated not only by the global surface temperature but also by radiation through other processes such as the diurnal cycle, precipitation, and other atmospheric components.

Recent studies have classified the mesoscale organization of marine shallow cumuli using satellite images into four states: sugar, gravel, fish, and flowers (Bony et al., 2020; Rasp et al., 2020; Stevens et al., 2020; Schulz et al., 2021). Sugar clouds are small and shallow, and reflect the least amount of solar radiation among these four states. Gravel clouds exhibit arc-shaped forms. Fish occurs in an elongated structure with distinct cloudy and clear-sky portions. Flowers are circular and often appear in multiple aggregates surrounded by dry areas, hence often referred to as a plural. Flowers usually have the highest cloud fraction among these four organization types.

Previous studies show that cloud organization and cloud amount are tightly connected with precipitation. To understand the precipitation formation of shallow cumuli, the Rain in Cumulus over the Ocean (RICO) project was deployed using surface observations, ship-based measurements and research aircrafts over the Atlantic Ocean in November 2004 - January 2005 (Rauber et al., 2007). A higher amount of moisture in the boundary layer promotes deeper clouds that contain higher cloud liquid water, hence often rain more, reducing the cloud amount (Nuijens et al., 2009, 2017). Some studies suggest that the mesoscale organization of shallow cumuli can accelerate the precipitation onset, further depleting the clouds (vanZanten et al., 2011; Bretherton & Blossey, 2017). Precipitation also leads to the formation of cold pools, which are mesoscale patterns of arc-shaped

clouds surrounding the regions of colder air and precipitating downdrafts (Zuidema et al., 2012, 2017). Some studies suggest that cold pools themselves are a dominant mechanism that leads to mesoscale cloud organization (Seifert & Heus, 2013).

Boundary layer radiative heating or cooling also modulates the depth, brightness, organization, and other properties of the clouds. Sufficiently strong boundary-layer radiative cooling can lead to a cooler boundary layer that modulates the depth of the shallow circulation (Naumann et al., 2017). Extra boundary-layer radiative cooling, even with increased sea surface temperature, can increase the cloud fraction through stronger downward entrainment heat flux carried by enhanced updraft mass flux (Narenpitak & Bretherton, 2019). Another factor that modulates the radiative heating or cooling rate, and evident even in the current climate, is the diurnal cycle. Vial et al. (2019, 2021) found that shallow cumulus clouds are thicker at night, due to cooler temperature associated with the lack of solar radiation. The surface wind speed is also often stronger at night, driving stronger surface latent heat flux that deepens the cloud layer, enhancing the entrainment of warmer air downward and further reducing the surface sensible heat flux (Nuijens & Stevens, 2012; Vial et al., 2021).

The depth of shallow cumulus clouds and its variation also depend on whether the clouds precipitate. Vial et al. (2019) found that non precipitating shallow cumuli grow during the day and reach the maximum vertical extent during sunset. On the other hand, precipitating shallow cumuli grow deeper at night with a maximum before sunrise. Vial et al. (2021) further shows that different mesoscale organization states also occur at different times of the day and can affect both the cloud depth and cloud fraction. Gravel and flowers often occur at night in deeper boundary layers, while sugar and fish are often observed during the day where the boundary layers are shallower. The time of day in which different cloud organization patterns occur contributes more to the daily variation of cloud fraction and cloud depth, rather than the diurnal variation of the same cloud organization pattern.

Aerosol can also modulate the radiation and indirectly affect the cloud properties. The aerosol-radiation interactions alter the planetary albedo, further changing the conditions of the boundary layer in which shallow clouds are formed. Multiple field campaigns were conducted to study the cloud-radiation and aerosol-radiation interactions in the past decade. The Cloud Systems Evolution in the Trades (CSET) field campaign

used the National Science Foundation and National Center for Atmospheric Research Gulfstream V (HIAPER) to study the evolution of the boundary layer aerosol, cloud, and thermodynamic structures in the trade wind regions over the north-Pacific Ocean in July-August 2015 (Albrecht et al., 2019). The Layered Atlantic Smoke Interactions with Clouds (LASIC) used the surface-based observations from the Atmospheric Radiation Measurement (ARM) Mobile Facility (AMF) to study trade-wind shallow cumuli near Ascension Island offshore of Africa between July 2016–October 2017 (Zuidema et al., 2018). The most recent field campaign that combined the studies of shallow cumulus clouds, aerosol, boundary layer structure, and large-scale meteorological and oceanic conditions altogether was the U.S. Atlantic Tradewind Ocean-Atmosphere Mesoscale Interaction Campaign (ATOMIC) and the European multinational Elucidating the Role of Clouds-Circulation Coupling in Climate field observation (EUREC^{4}A), which took place in January-February, 2020, over the Atlantic Ocean near Barbados (Bony et al., 2017; Quinn et al., 2021; Pincus et al., 2021; Stevens et al., 2021; Stephan et al., 2021; Bony et al., 2022).

During the ATOMIC and EUREC^{4}A field campaign, there were several days when mineral dust, black carbon, biomass burning, and other aerosol species were observed in the region, enabling studies of the interactions between clouds and aerosol (Quinn et al., 2021; Bony et al., 2022). The four mesoscale organization patterns of shallow cumuli were observed throughout the field campaign period, and transitions between the cloud patterns took place (Pincus et al., 2021; Stevens et al., 2021; Schulz, 2021; Bony et al., 2022; Narenpitak et al., 2021). In particular, on February 2-3, 2020, a transition from sugar to flower shallow cumulus clouds was observed near Barbados over the course of less than 24 hours. Between January 31 and February 3, an aerosol layer consisting mainly of mineral dust was observed above the clouds, resulting in an aerosol optical depth of approximately 0.35 (Quinn et al., 2021). Narenpitak et al. (2021) simulated this sugar-to-flower (S2F) transition event and determined the mechanism of the transition using the System for Atmospheric Modeling (SAM) as a large eddy simulation (LES), driven with reanalysis data based on the approach in Kazil et al. (2021). In Narenpitak et al. (2021), the mechanism responsible for the S2F transition is the mesoscale circulation associated with the shallow cumulus plumes that renders the moist and cloudy areas moister, and dry areas drier. The organization is strengthened further when the cloud system ex-

periences stronger large-scale upward motion, as the deepened cloud layer carries larger and stronger mesoscale circulation that accelerates the organization.

Using the results from LES together with the ship-based measurements, Narenpitak et al. (2021) quantified the amount of surface radiation flux modulated by the mineral dust layer at the location of the National Oceanic and Atmospheric Administration's (NOAA) Research Vessel Ronald H. Brown (RHB), which was stationed at 54.5°W and 13.0°N during the dusty period. The mineral dust reduces the amount of downward solar radiation reaching the RHB (their Fig. A3). This work extends Narenpitak et al. (2021) to study the cloud-radiation interaction and the aerosol-radiation interaction in the context of the S2F transition. The first part examines the role of the diurnal cycle on the S2F transition, precipitation, and the cloud and cold pool dynamics. The second part examines the role of free-tropospheric mineral dust on radiation and its impacts on the transition and organization of the clouds.

The organization of this paper as as follows. Section 2 describes the configuration of the simulations and the data used from the field campaign. Section 3 describes mathematical equations used to quantify the strength of cloud organizations and to detect the cold pools. Section 4 analyses the impacts of diurnal cycle on the S2F transition. Section 5 explores the impacts of free-tropospheric mineral dust on the clouds. Finally, Section 6 presents the conclusions.

2 Data and Simulations

The System for Atmospheric Modeling (SAM) (Khairoutdinov & Randall, 2003) is employed to simulate the transition from sugar to flower shallow cumuli observed on February 2-3, 2020, during the ATOMIC and EUREC^{4}A field campaign. The simulations are driven with the large-scale forcings from the European Center for Medium-Range Weather Forecasts (ECMWF) Reanalysis 5^{th} Generation (ERA5) (Hersbach et al., 2020), following a boundary-layer air mass that passes over the RHB at 13:00 local time (17 UTC) on February 2, 2020. The trajectory was calculated by the Hybrid Single-Particle Lagrangian Integrated Trajectory (HYSPLIT) model (Rolph et al., 2017; Stein et al., 2015) with the initial point from the RHB at 500 m altitude forward and backward in time to construct a time-height curtain of the large-scale atmospheric conditions. The greenhouse gas concentration profiles of carbon dioxide, methane, nitrous oxide, and ozone

Table 1. Major configuration differences in the three sugar-to-flower (S2F) transition simulations

Simulations	Time of the cloud transition	Diurnal cycle	Mineral dust
Control (Daytime / NoDust)	Daytime	Directly from ERA5 (22:00 - 22:00 local time)	None
Nighttime	Nighttime	Shifted 12 hours later from ERA5 (10:00 - 10:00 local time)	None
Dust	Daytime	Directly from ERA5 (22:00 - 22:00 local time)	Initialized between 4 km and 5.5 km (1600 mg^{-1} concentration, AOD $\approx$ 0.35)

are based on the Community Earth System Model version 1 (CESM1) (Hurrell et al., 2013) Whole Atmosphere Community Climate Model (WACCM) (Marsh et al., 2013). The ensemble-mean outputs are from the CESM1-WACCM simulations initialized following the representative concentration pathway 8.5 (RCP8.5, a high anthropogenic emission scenario). The greenhouse gas concentration profiles averaged from January-February of 2016 through 2025 over 10.42°N-21.79°N and 295°E-310°E are used to represent the current climate over the Atlantic Ocean. Unless otherwise noted, the other details of the simulation configurations are as described in Section 2 of Narenpitak et al. (2021).

Three simulations are presented in this paper, as summarized in Table 1. All of them are configured with horizontal grid spacing of 100 m and a horizontal domain extent of 192×192 km^2. The vertical grid spacing is 50 m, increasing geometrically from 5 km to 10 km, which is the domain top. There are 125 vertical levels in total. Above the model top, the atmospheric profiles from ERA5 and greenhouse gas concentrations from CESM1-WACCM are used up to the top of the atmosphere for the radiation calculation. As in

Narenpitak et al. (2021), the simulations use a two-moment bin-emulating bulk microphysics scheme (Feingold et al., 1998) and the Rapid Radiative Transfer Model for global climate model applications (RRTMG) (Mlawer et al., 1997) with time varying atmospheric profiles above the domain top and the diurnal cycle of solar radiation. The radiation is computed every 10 s. The model time step is 2 s, and the duration of the simulations is 24 hr.

The primary aerosol type in all of these three simulations is sea-salt particles. The simulations are initialized with a bimodal sea-salt aerosol distribution in the boundary layer, based on the shipboard measurement from the RHB (Quinn et al., 2021). The sea-salt aerosol size distribution is shown in Figure A2 of Narenpitak et al. (2021). The fine mode sea-salt aerosol (with a geometric mean diameter of 0.13 μm and a geometric standard deviation of 1.71) has a concentration of 400 mg^{-1}, and the coarse mode aerosol (with a geometric mean diameter of 0.96 μm and a geometric standard deviation of 1.73) has a concentration of 13 mg^{-1}. The initial sea-salt aerosol concentration in the free troposphere is 32 mg^{-1}, consistent with the EUREC^{4}A measurements from the Ultra-High-Sensitivity Aerosol Spectrometer (UHSAS) and the Cloud Droplet Probe (CDP-2) on the French ATR-42 research aircraft (Coutris & Ehses, 2021; Bony et al., 2022). The sea-salt particles are coupled with the cloud microphysics scheme.

2.1 The impact of diurnal cycle on the moisture aggregation

Two simulations are used to assess the impact of the diurnal cycle on the S2F transition: the Daytime (or Control) and the Nighttime simulations. The Daytime simulation represents the S2F transition observed on February 2-3, 2020, except without a mineral dust layer initialized in SAM. The insolation time series from the Daytime simulation follows the insolation along the forcing trajectory derived from ERA5 (Fig. 1a, blue line). The S2F transition occurred during the day of February 2 local time, so the control simulation is referred to as the Daytime simulation when discussed in the context of the diurnal cycle impact. The Daytime simulation is from 22:00 on February 1 to 22:00 on February 2, local time.

The Nighttime simulation examines the impact of the diurnal cycle on the S2F transition, as if the transition had occurred during the nighttime. The insolation time series used to drive the simulation is still from ERA5 but shifted later by 12 hours (Fig. 1a,

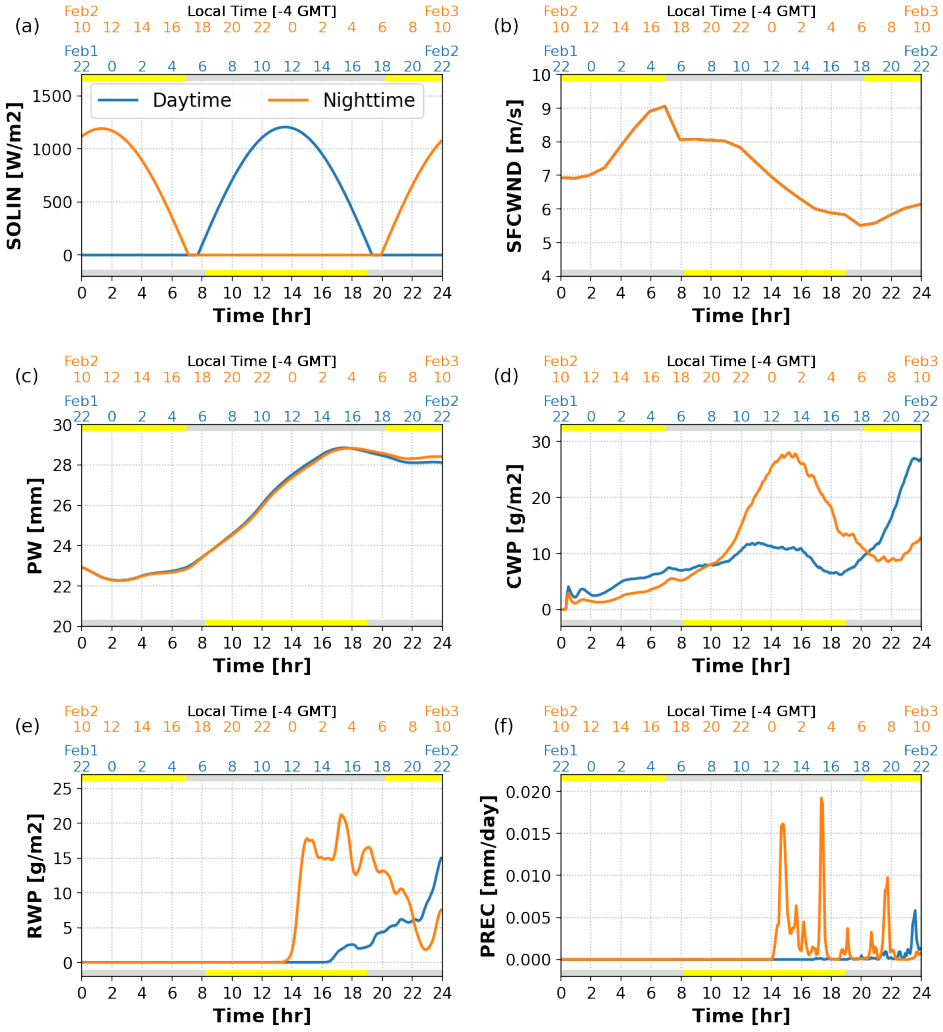

Figure 1. Domain-mean time series of various variables from the daytime-transition (Daytime) and nighttime-transition (Nighttime) simulations (blue and orange, respectively): (a) insolation, (b) surface wind speed, (c) precipitable water, (d) cloud water path, (e) rain water path, and (f) surface precipitation. The bottom x-axes indicate time after the simulations begin, while the top x-axes indicate the local time of both simulations, relative to the insolation. Other large-scale forcings aside from the insolation are kept identical. The gray band indicates the night and the yellow band indicates the day (insolation greater than zero). The bottom (top) band is for the Daytime (Nighttime) simulation.

orange line), so the simulation is run from 10:00 on February 2 to 10:00 on February 3, local time. Aside from the shifted diurnal cycle, everything else from the large-scale meteorology of ERA5 remains the same. The results of these two simulations are presented in Section 4.

2.2 The radiative impact of mineral dust on the moisture aggregation

Two simulations are used to assess the impact of mineral dust in the free troposphere on the S2F transition: the NoDust (same as Control) and the Dust simulations. The Dust simulation examines the radiative impacts of the mineral dust on the moisture aggregation and the transition of the clouds. Between February 2-3, 2020, a layer of mineral dust was observed above the cloud layer near Barbados (Quinn et al., 2021; Bony et al., 2022). To represent the observed dust layer, an additional aerosol species is included in SAM. A mineral dust layer with a concentration of 1600 mg^{-1} is initialized between 4 km and 5.5 km, colocated with an elevated moist layer (Gutleben et al., 2019), as described in the Appendix A2 of Narenpitak et al. (2021). The mineral dust optical properties are calculated based on the assumed size distribution and refractive indices in d'Almeida et al. (1991). The dry aerosol single scattering albedo is 0.85 in the visible part of the spectrum. The aerosol optical depth at this time is approximately 0.35, consistent with the Moderate Resolution Imaging Spectroradiometer (MODIS) observation at this time.

The mineral dust is advected in all directions and allowed to spatially and temporally vary the radiative heating rate. The local heating rate of the mineral dust is computed using a look up table of wavelength dependent optical properties (single scattering albedo, asymmetry parameter, and extinction coefficient) of dry mineral dust aerosol with the size distribution measured during ATOMIC (Quinn et al., 2021). The assumption of dry particles is consistent with the low (< 15 %) relative humidity in the free troposphere in the simulations, where the mineral dust layer is located. The mineral dust is coupled with the radiation scheme, but not with the cloud microphysics scheme, because the mineral dust layer resided above the boundary layer.

In addition to the original output variables from SAM, the radiative fluxes and radiative heating rates (both solar or shortwave and infrared or longwave radiation) from the atmosphere without mineral dust are also calculated. Thus, the radiative heating due

to the mineral dust can be directly obtained by subtracting the total radiative fluxes (and heating rates) from those of the atmosphere without mineral dust. These variables are useful for determining the effects of the mineral dust on the radiation and the moisture aggregation in Section 5.

3 Methods

3.1 Scale partitioning

Narenpitak et al. (2021) examined the mechanism responsible for the moisture aggregation in their simulations. Following Bretherton and Blossey (2017), the simulation output is partitioned into contributions from the large scale, mesoscale, and cumulus scale. The scale partitioning can be performed on any variable fields. Consider, for example, the vertical velocity output at a particular time $w(x, y, z, t)$; the partitioning of vertical velocity is given by:

$$w(x, y, z, t) = \overline{w}(z, t) + w''(x_m, y_m, z, t) + w'''(x, y, z, t) \quad . \tag{1}$$

The over-line indicates the domain average, representing the large-scale contribution. The double prime indicates the perturbation from the domain average, coarse-grained to a tile size that is representative of the mesoscale (x_m, y_m), such as 16 km. The quantity represents the variability associated with the mesoscale perturbation. The triple prime term is the residual, which represents the variability associated with the cumulus-scale process. Unless otherwise specified, the tile size of 16 km is used for coarse-graining and computing the mesoscale contribution. Readers are referred to Section 3.1 and Appendices B and D1 of Narenpitak et al. (2021) for details.

The term $w''(x_m, y_m, z, t)$ represents the mesoscale vertical velocity perturbation relative to the domain average. When positive, $w'' > 0$ indicates that there is local (mesoscale) ascent in the considered mesoscale tile. Mass continuity requires that there is local convergence below and local divergence aloft in the areas where $w'' > 0$. The w'' profiles can be sorted by the total water path (TWP, a sum of water vapor, cloud water and rain water paths) at every time step, and averaged into quartiles of TWP. The lowest TWP quartile (Q1) represents the driest and cloud-free regions; whereas the highest TWP quartile (Q4) represents the moist and cloudy regions. The mesoscale tiles in these quartiles are not necessarily adjacent to one another.

3.2 The mesoscale total water perturbation budget

As found in Bretherton and Blossey (2017) and Narenpitak et al. (2021), the mesoscale circulation mentioned above is responsible for aggregating the total water in the non-precipitating shallow cumuli, rendering the moist areas moister and the dry areas drier. The process can be mathematically explained using the budget of mesoscale total water perturbations or q_t'':

$$q_t''(x_m, y_m, z, t) = \mathcal{A} + \mathcal{F} + \mathcal{C} + \mathcal{S} \quad . \tag{2}$$

It consists of four main processes: the advection of q_t'' due to the large-scale and mesoscale winds ($\mathcal{A}$), the horizontal and vertical gradients of the cumulus-scale total water flux ($\mathcal{F}$), the mesoscale vertical advection of large-scale total water ($\mathcal{C}$), and the mesoscale perturbations of the precipitation mass flux divergence ($\mathcal{S}$). The details are described in Appendix B.

Bretherton and Blossey (2017) found that, $\mathcal{C}$ dominates the q_t'' budget of shallow cumulus organization in the Pacific Ocean. Narenpitak et al. (2021) further found that, although the S2F transition is a different cloud regime than those observed over the Pacific Ocean, $\mathcal{C}$ still dominates the q_t'' budget in the non-precipitating flower aggregates observed over the Atlantic.

The $\mathcal{C}$ term will be referred to and shown throughout the rest of this paper. Because of mass continuity, the mesoscale vertical advection of the large-scale total water,

$$\mathcal{C} = -w'' \frac{\partial \overline{q_t}}{\partial z} \quad , \tag{3}$$

can be physically interpreted as a mesoscale convergence or divergence (as represented by w'') of the large-scale total water gradient ($\frac{\partial \overline{q_t}}{\partial z}$). Since the large-scale total water $\overline{q_t}$ decreases with height, it follows that $\mathcal{C} > 0$ when $w'' > 0$, or when there is local convergence below and divergence aloft. When $\mathcal{C}$ is vertically integrated, it represents the net convergence or divergence of total water. If $\int \mathcal{C} \mathrm{d}z > 0$, there is net convergence of total water in the considered mesoscale region, which will then become moister with time. The considered mesoscale region becomes more moist when there is net convergence of total water.

3.3 Organization diagnostics

Three organization diagnostics are used in this paper: the mean area of cumulus aggregates, the cloud aggregate counts, and the normalized standard deviation of TWP. An algorithm is developed to detect the cloud aggregates of adjacent pixels with the total (cloud and rain) optical depth exceeding 1. The area of the cloud aggregates is, therefore, a factor of the simulation grid size or 100×100 m^2. Larger cloud aggregate areas and fewer aggregate counts mean the mesoscale organization is stronger. The normalized standard deviation of TWP is the ratio of the TWP standard deviation (σ_{TWP}) divided by the domain-mean TWP ($\overline{TWP}$). Greater normalized TWP standard deviation also implies stronger organization, as the dry areas become drier and the moist areas become moister.

3.4 Cold pool detection

Shallow cumulus cold pools are regions of colder air, surrounded by warmer air, associated with evaporative downdrafts of significant precipitation from shallow cumulus clouds (Rauber et al., 2007; Zuidema et al., 2017). As the cold air reaches the surface, it creates a density current pushing the air outward forming a mesoscale circular edge. The air along the gust front can create a second cycle of convection, forming new clouds at the edge of the cold pools. With this definition, a sharp drop in the near-surface or subcloud-layer temperature is used to identify the cold pools.

Cold pools are found in all of these three simulations after the precipitation onset. In this study, cold pools are detected using a threshold of the surface virtual potential temperature (Θ_v). The threshold computed using the instantaneous output of Θ_v at the respective time is:

$$\tilde{\Theta}_v - \sigma_{\Theta_v},$$

where $\tilde{\Theta}_v$ is the median of the surface Θ_v in the entire domain, and σ_{Θ_v} is the standard deviation of the surface Θ_v within the domain. Any grid cell with Θ_v below the threshold is considered part of the cold pools.

The cold pools can also be determined by the surface divergence and convergence. The surface divergence term ($\mathcal{D}iv$) is computed from 2-km coarse-grained horizontal wind

fields at the surface:

$$\mathcal{D}iv = \left[\frac{\partial u_s}{\partial x}\right]_{2km} + \left[\frac{\partial v_s}{\partial y}\right]_{2km} \quad . \tag{4}$$

The areas in which $\mathcal{D}iv > 1 \times 10^{-6}$ s^{-1} are in precipitating downdrafts. The contours where $\mathcal{D}iv < -1 \times 10^{-6}$ s^{-1} indicate areas where there is strong surface convergence associated with the gust front or the cold pool edges. Cold pools with stronger downdrafts and surface divergence are often associated with a deeper temperature drop (Vogel et al., 2021). See Figures 3-4 and 10 for examples.

4 The Impacts of Diurnal Cycle on the S2F Transition

4.1 Diurnal cycle and the transition from sugar to flower shallow cumuli

This section focuses on the impact of the diurnal cycle on the S2F transition. Figure 1 shows the evolution of the shallow cumulus clouds in the Daytime (blue) and Nighttime (orange) simulations. They are both driven with the same large-scale meteorological forcings, except the diurnal cycle in the Nighttime simulation is shifted by 12 hours later from the Daytime simulation (Fig. 1a). Prior studies stated that at night, the surface wind speed of the shallow cumulus clouds is often stronger than during the day, leading to stronger surface latent heat flux, deeper clouds, and higher cloud amount (Nuijens & Stevens, 2012; Vial et al., 2021). For the Daytime and Nighttime simulations, the surface wind speed is kept identical (Fig. 1b) to eliminate the potential consequences of this factor. Figure 1c-f shows that the Nighttime simulation produces more cloud and rain water than Daytime. Although the precipitable water (PW, or the column integrated water vapor) gradually increases from hours 6 to 16, the cloud and rain water are maximized at night in each simulation, regardless of the surface wind speed, surface latent and sensible heat fluxes, and the Bowen ratio (Fig. A1).

Figures 2-4 show that the S2F transition in the Nighttime simulation occurs more rapidly than the transition in Daytime. In both simulations, the cloud layers are both initially shallow. They similarly deepen rapidly during hours 10-12 because of a strong upward motion in the large-scale forcings (Fig. 3b in Narenpitak et al. (2021)). The maximum cloud top height is slightly higher in the Nighttime simulation, and the cloud tops reach their maximum heights during hours 16-18 in both simulations. The cloud and rain amounts in the Nighttime simulation reach their maximum values 12 and 6 hours sooner,

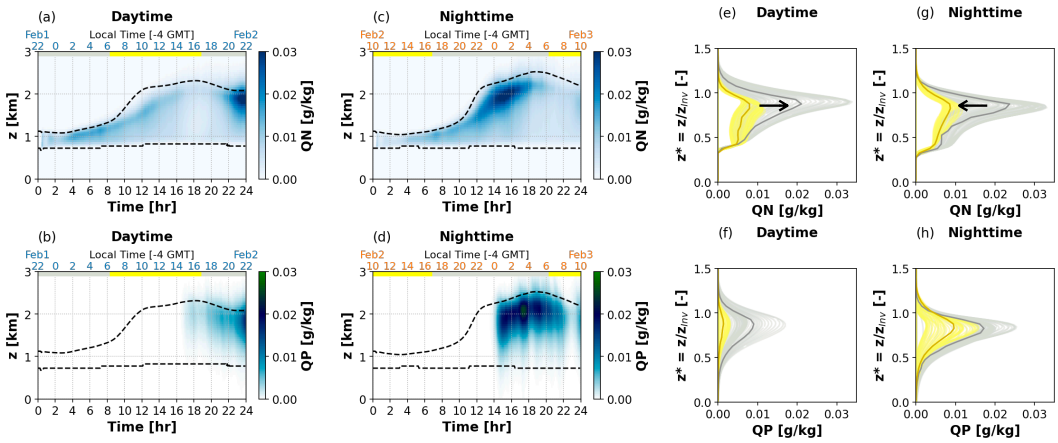

Figure 2. Domain-mean time series and vertical profiles of (top) cloud water mixing ratio (QN) and (bottom) rain water mixing ratio (QP) from the Daytime and Nighttime simulations. (a-b) Time series of QN and QP from Daytime; the lower x-axes indicate time after the simulations begin and the upper x-axes indicate the local time of the Daytime simulation. The gray and yellow band indicate nighttime and daytime, respectively. (c-d) As in panels (a-b) but for the Nighttime simulation. (e-f) Vertical profiles of domain-mean QN and QP from Daytime after 14 hours (last 10 hours of the simulations) plotted against the normalized height or z^*, which is the ratio between the physical height (z) and the domain-mean inversion height (z_{Inv}) of the respective simulations. The gray (yellow) color represents profiles during the nighttime (daytime). The average profiles during the nighttime (daytime) are plotted in dark gray (dark yellow). Panels (g-h) are as in (e-f) but for the Nighttime simulation. The black arrows in panels (e) and (g) point from the earlier times (lower precipitable water) to the later times (higher precipitable water).

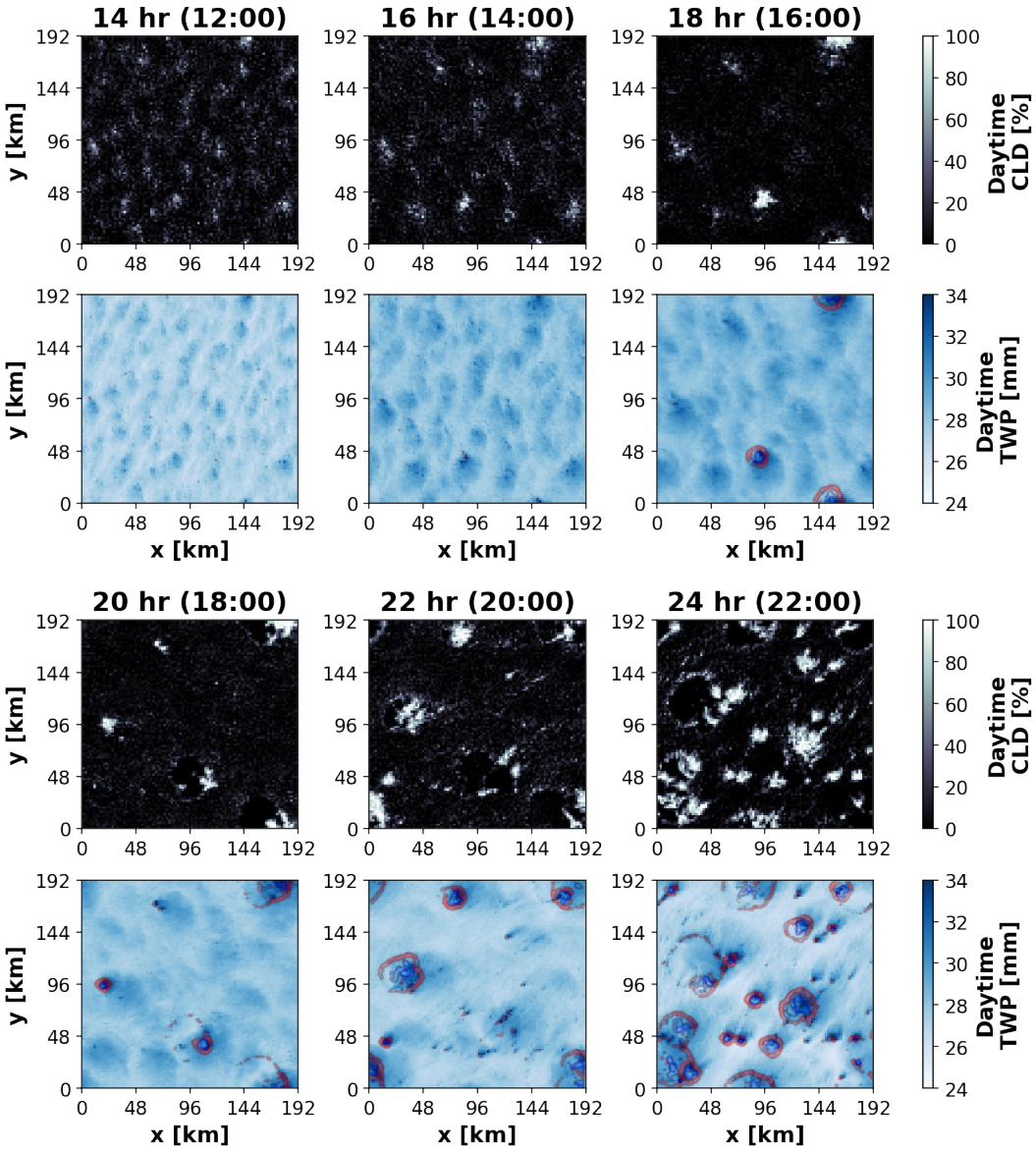

Figure 3. Snapshots of (top) cloud fraction (CLD) and (bottom) total water path (TWP, which is a sum of water vapor, cloud and ran water paths), showing the transition from sugar to flower shallow cumuli from the Daytime simulation. The snapshots are plotted every other hour during the last 12 hours of the simulation (12:00 to 22:00, local time). The red and blue contour lines on the TWP snapshots show areas where the magnitudes of surface convergence (red contours) and surface divergence (blue contours) are stronger than 10^{-6} s^{-1}. The areas with surface divergence correspond to the precipitating downdrafts associated with the clustered shallow cumuli and the rings of surface convergence correspond to the edges of cold pools.

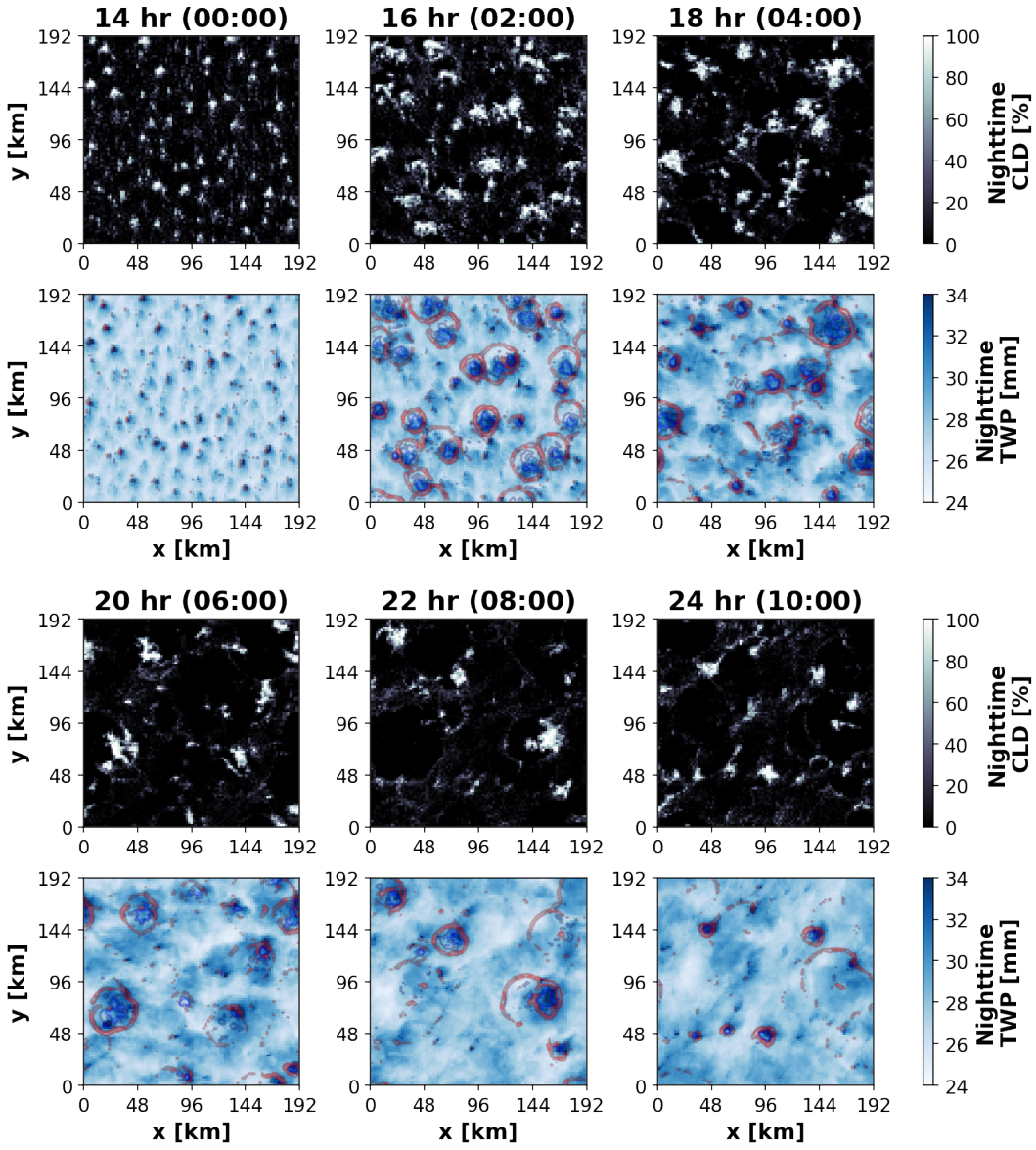

Figure 4. As in Figure 3 but for the Nighttime simulation. The snapshots are from 0 am to 10 am, local time.

respectively, compared to the Daytime simulation (Fig. 2a-d). The snapshots of the cloud fraction (CLD) and TWP in Figures 3-4 show that as the aggregated flower clusters precipitate, the cloud system produces a large number of cold pools beneath the clouds. The Nighttime simulation, which has stronger precipitation, also produces more cold pools.

The results so far clearly show that the Nighttime simulation produces larger flower clusters with more cloud liquid water and rain, with the only factor that is different between the Nighttime and Daytime simulations being the solar radiation. This is summarized by Figure 2e-h. The domain-mean output in the last 10 hours of both simulations are composited and plotted against the normalized height (z^*), which is the altitude (z) divided by the domain-mean inversion height (z_{Inv}) at each time. The yellow (gray) profiles are from the day (night). It is evident that the cloud liquid water and rain water of the aggregated shallow cumuli are greater at night, regardless of the large-scale water vapor in the forcings. The clouds are in a larger form of flower aggregates, as evident in the domain snapshots (Fig. 3-4) and the mean area of the cloud aggregate time series (Fig. 5a), and have larger cloud water mixing ratio at the top of the cloud layer, which is a key characteristic of the flower clouds (Bony et al., 2020). This feature is consistent with previous studies, such as Vial et al. (2019) and Vial et al. (2021) who showed that shallow cumuli are often deeper at night when the shortwave radiative heating is zero. Since the only difference in the model configuration is the shifted diurnal cycle, this study emphasizes that the solar radiation alone has a strong influence on the shallow cumulus cloud system.

The solar radiation not only affects the domain-mean quantities of the simulations but also has a strong influence on the distribution of moisture and clouds. Figure 3-4 show that the clouds and the total water in both simulations have aggregated into clusters surrounded by dry regions, especially at night. The clouds in the Nighttime simulation aggregate sooner than those in the Daytime simulation. As the clouds grow, they produce sufficient rain water, resulting in precipitating downdrafts that generate cold pools. The edges of the cold pools are indicated by red contours, which represent areas where convergence of the surface horizontal wind is stronger than 10^{-6} s^{-1}. The moisture aggregation is strongest and the cold pools are the most dense at night.

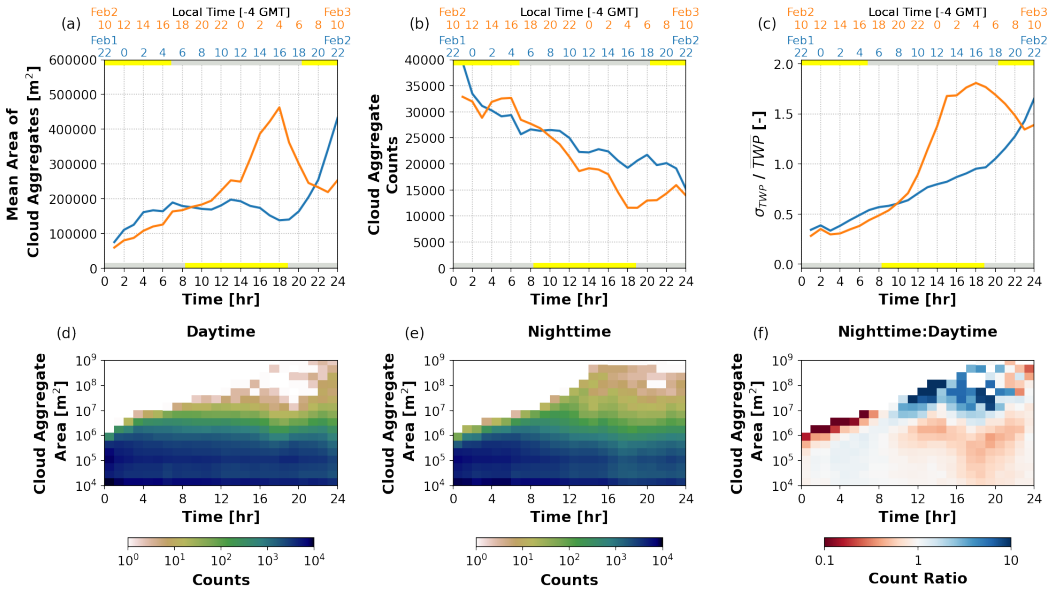

Figure 5. Time series of (a) the mean area of cumulus cloud aggregates, with a contiguous cloud optical depth exceeding 1 (QOPD > 1), (b) the cloud aggregate counts, and (c) the standard deviation of TWP normalized by the domain-mean TWP from the Daytime (blue) and Nighttime (orange) simulations. The x-axis labels are as in Figure 1. (d-e) Hourly distributions of the cloud aggregate areas from the Daytime and Nighttime simulations, plotted against time. (f) Ratio of the distributions of the cloud aggregate areas between the Nighttime and Daytime simulations. When the ratio is greater than one, the Nighttime simulation produces more aggregates of the respective cloud sizes than the Daytime simulation.

4.2 Diurnal cycle and the mesoscale aggregation of moisture and clouds

Figure 5a-c shows the hourly time series of various organization diagnostics: (a) the mean area of cloud aggregates, (b) the cloud aggregate counts, and (c) the normalized TWP standard deviation of both simulations. The time series clearly show that in the early morning, the Nighttime simulation produces the largest mean area of cloud aggregates (maximum of 450,000 m^2, or 45 pixels, at hour 18 or 4:00 local time) and the lowest aggregate counts (slightly above 10,000 aggregates). The normalized TWP standard deviation also increases rapidly and remains higher at night. These indicate the time of strongest mesoscale organization in the Nighttime simulation. On the other hand, the Daytime simulation takes longer to reach a similar maximal organization strength after hour 22, as it needs not only sufficient PW to produce clouds but also for the shortwave radiative heating to be zero and for the boundary layer to be cool enough for the clouds to deepen.

The distributions of the cloud aggregate areas plotted every hour are displayed in Figure 5d-e, and the the ratio of both histograms (Nighttime to Daytime) in Figure 5f. The ratio of the Nighttime to Daytime cloud aggregate area distributions suggest that, at night, between hours 8 and 22, the Nighttime simulation produces higher cloud aggregate counts with areas larger than $5{\times}10^6$ m^2, or 500 pixels. This clearly shows that the diurnal cycle has strong impacts on the rate of moisture aggregation in the mesoscale.

Figure 6 shows vertical profiles of the mesoscale vertical velocity perturbation relative to the domain averages (w'') and the convergence of total water due to mesoscale circulation ($\mathcal{C}$, see Equations 2-3). They are sorted by TWP and averaged into quartiles of TWP at respective times. The highest TWP quartile or Q4 represents the top 25% of the moistest and cloudiest regions in the Daytime and Nighttime simulations (dark blue lines). The time-height curtains of $\mathcal{C}$ from the highest TWP quartile are shown at bottom. The vertical profiles of w'' from the Daytime simulation (Fig. 6a-e, dashed lines) are consistent with the finding in Figure 4 of Narenpitak et al. (2021). As the sugar clouds transition into the flower clouds, there is local ascending (descending) air in (above) the mesoscale cloud plumes, and local descending air in the surrounding dry regions. Mass continuity implies that there is local convergence below the mesoscale cloud plumes, and local divergence above. Further analysis of the mesoscale total water perturbation (q_t'') budget shows that there is an overall convergence of total water in the cloud layer of the

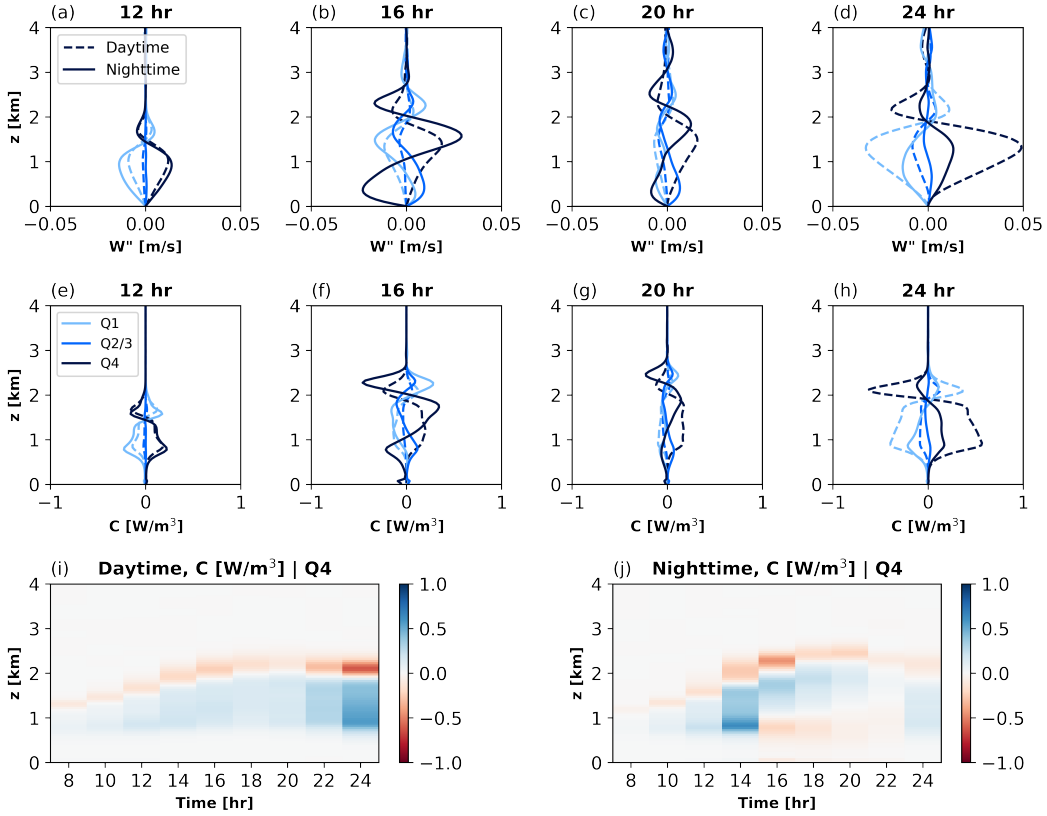

Figure 6. Vertical profiles of (a-d) the mesoscale perturbation of vertical velocity from the domain averages (w'') and (e-h) the moisture convergence due to mesoscale circulation ($\mathcal{C}$) from the Daytime and Nighttime simulations, plotted at various times. The profiles are sorted by the total water path or TWP at the respective times and averaged into four TWP quartiles, Q1 being the lowest quartile (driest, light colors) and Q4 being the highest (moistest, dark colors). The profiles from Q2 and Q3 are averaged. (i-j) Time-height curtains of $\mathcal{C}$ from the highest TWP quartile from the Daytime and Nighttime simulations.

already moist and cloudy regions of the Daytime simulation ($\mathcal{C} > 0$), allowing the moisture aggregation to strengthen and the cloud clusters to grow (Fig. 6e-h, and i). See Appendix A1 and Figure B of this paper for the other terms in the q_t'' budget equation.

In contrast, the results from the Nighttime simulation show that when the shallow cumuli are heavily precipitating (hours 16-20), the convergence of total water due to mesoscale circulation computed at a 16-km mesoscale tile is negative in the subcloud layer. The w'' and $\mathcal{C}$ terms are still positive in the cloud layer of Q4, suggesting that there is still local convergence of moisture into the cloud plumes. However, when the cold pools form, the surface divergence associated with precipitating downdraft beneath the clouds removes the moisture from the moist regions below the cloud plumes. This is evident in Figures 6f-g and 6j.

An argument is made that the $\mathcal{C}$ term is still responsible for moistening the moist columns follows, but over a smaller scale. Instead of using 16 km, the scale of the moist columns needs to be adjusted such that they are smaller than the size of the cold pools to see this effect. The column-integrated mesoscale moisture convergence is negative between hours 16-20 in Q4 when a 16-km tile size is used for the q_t'' budget (Fig. 6f). However, it is still positive if smaller tile sizes (6.4 km or smaller) are used (Fig. B4d). Figures B4-B5 show that, at the center of the cold pools where precipitating downdrafts are present, the mixed-layer total water divergence ($\mathcal{C} < 0$) is compensated by the upward vertical advection of total water perturbations $\mathcal{A}_v > 0$. At the edges of the cold pools, there is mixed-layer total water convergence ($\mathcal{C} > 0$). The edges of the cold pools are originally drier and cloud-free. But with the newly transported total water, these areas have sufficient moisture for new convection to form. This is consistent with the snapshots of the Nighttime simulation at hours 16-18 (Fig. 3). When flower clouds precipitate more heavily, they produce cold pools with stronger precipitating downdrafts, leading to gust fronts that encourage the next generation of flower clouds to grow. As the new convection takes place, the old cold pools dissipate. These cloud and cold pool interactions observed in the Nighttime simulation are consistent with previous findings (Zuidema et al., 2012, 2017). Such dynamics need sufficiently high resolution in order to be adequately represented.

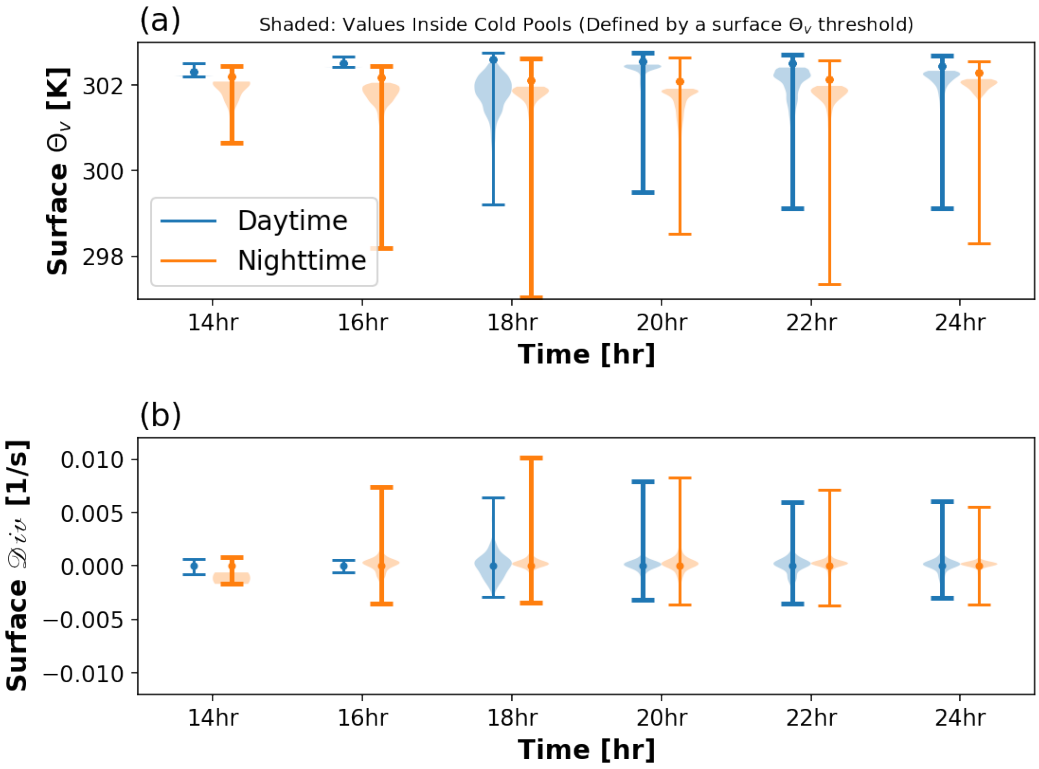

Figure 7. Distributions of (top) the surface virtual potential temperature (Θ_v) and (bottom) the surface divergence term ($\mathcal{D}iv$) every two hours from the Daytime (blue) and Nighttime (orange) simulations. The thick lines indicate a night time of the corresponding simulation. The shaded areas show the distributions (by density) of surface Θ_v and $\mathcal{D}iv$ inside the cold pools. The short horizontal lines represent the minima and maxima, and the dots represent the medians. The histograms are plotted every 2 hours from hours 14 to 24.

4.3 Diurnal cycle and the cold pools

Figure 7 further elucidates the cloud-precipitation-cold pool interactions and the differences that occur between night and day. The distributions of (a) the surface virtual potential temperature (Θ_v), and (b) the surface divergence ($\mathcal{D}iv$) (see Equation 4) are presented. The surface Θ_v term is used as a proxy for the surface buoyancy; lower surface Θ_v means less buoyancy and stronger cold pools (Vogel et al., 2021). The positive $\mathcal{D}iv$ term represents the strength of the precipitating downdraft and the gust front, a density current that carries the moisture outward, lifting the air in the mixed layer, forming new convection (Zuidema et al., 2012). The shaded areas show Θ_v and $\mathcal{D}iv$ inside the cold pools. The distributions are shown starting from hours 14, when significant precipitation generates cold pools in the Nighttime simulation. It is clear that cold pools developed in the Nighttime simulation are stronger, even when compared with the cold pools that develop at night of the Daytime simulation. The associated gust fronts also lead to new convection that grows into a second generation of flower clouds that later precipitate and also form new cold pools.

5 The Radiative Impacts of Mineral Dust on the S2F Transition

Mineral dust was present above the cloud layer when the sugar-to-flower transition took place on February 2-3, 2020. The mineral dust layer was advected from Africa over to the Caribbean (Quinn et al., 2021; Bony et al., 2022). It is of interest to examine the interactions between radiation and mineral dust, and to determine whether the mineral dust in the free troposphere affects the transition from sugar to flowers. An additional simulation is performed. In the Dust simulation, a mineral dust layer is initialized at the beginning with a concentration of 1600 mg^{-1} between 4 and 5.5 km, equivalent to an aerosol optical depth of 0.35. The differences in radiation caused by the mineral dust layer are shown in Figure 8a-b, which presents the time series of the domain-mean net shortwave and longwave radiation at the surface (SWNS and LWNS, respectively) of the NoDust (control) and Dust simulations. The mineral dust layer reduces the net shortwave radiation at the surface during the day, with a maximum of 65 W m^{-2} around noon local time. The mineral dust also reduces the net longwave radiation at the surface by 1.7 W m^{-2} on average throughout the simulation.

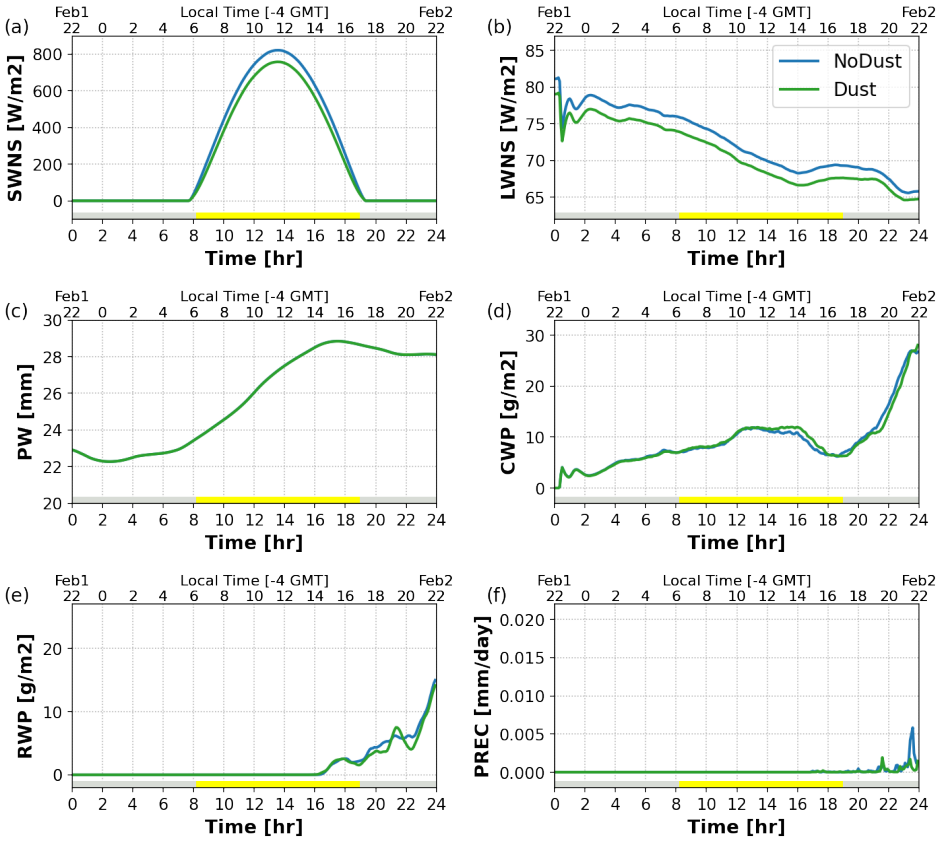

Figure 8. Domain-mean time series of various variables from the simulation without dust (NoDust, blue) and the simulation with dust (Dust, green): (a) net surface shortwave radiative flux, (b) net surface longwave radiative flux, (c) precipitable water, (d) cloud water path, (e) rain water path, and (f) surface precipitation. The bottom x-axes indicate time after the simulations begin, while the top x-axes indicate the local time of both simulations (same local time for both). The gray and yellow bands represent nighttime and daytime, respectively, shown at the bottom of each panel.

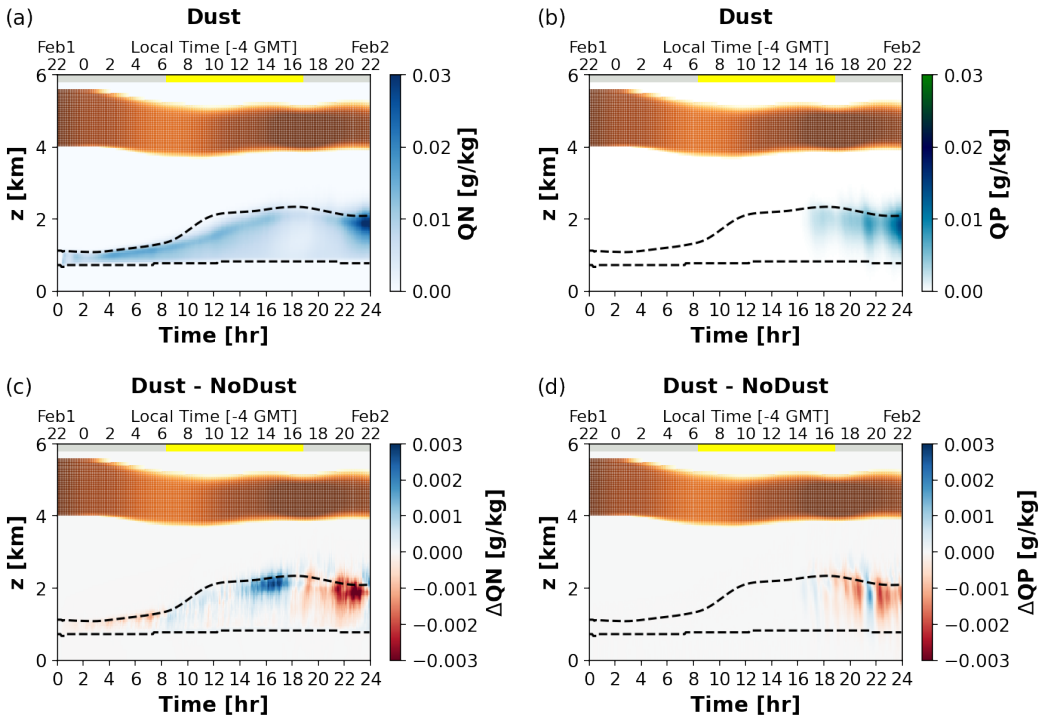

Figure 9. Domain-mean time series of (a-b) cloud and rain water mixing ratios (QN and QP, respectively) from the Dust simulation. (c-d) Differences in QN and QP between the Dust and NoDust simulations. The black dashed lines indicate the cloud top and base heights of the Dust simulation. The brown shading indicates the mineral dust layer. The bottom x-axes indicate the time after the simulations begin and the top x-axes indicate the local time of the simulations, as in Figure 2.

5.1 Free-tropospheric mineral dust and the transition from sugar to flower shallow cumuli

The vertical structures and the differences of the cloud and rain water are shown in Figure 9. Since the only difference between these two simulations is the presence of mineral dust above the cloud, it is expected that the precipitable water remains the same in both simulations (Fig. 8c). Before sunrise, the Dust simulation produces slightly less cloud condensates than the NoDust simulation. The Dust simulation then produces slightly more cloud condensate than NoDust during the day, especially in the afternoon (hours 14-18), and the NoDust simulation catches up again after sunset (Fig. 8d and 9c). There is marginal difference in rain water path and surface precipitation; in general, the Dust simulation produces less rain than the NoDust counterpart as the rain occurs at night

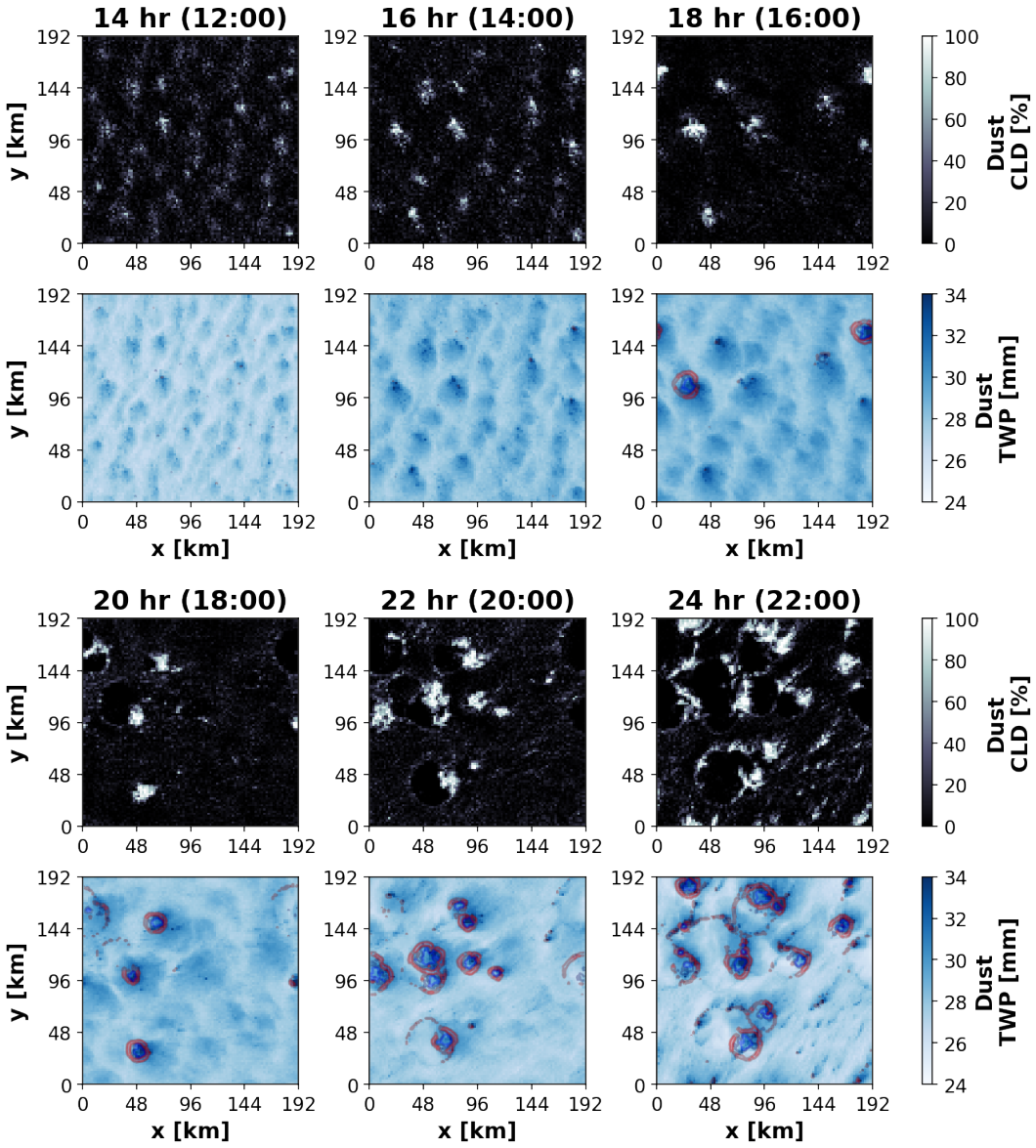

Figure 10. As in Figure 3 but for the Dust simulation. The local time of the Dust simulation is the same as the NoDust (Control) simulation. There are more cold pools relative to Figure 3.

when the Dust simulation produces slightly less clouds. Further discussion is deferred to Section 5.2.

When considering the spatial distribution of the clouds (Fig. 3 and 10), there are noticeable differences in the patterns and the rates of cloud organization between NoDust and Dust. Particularly, there are more flower clouds in the Dust simulation between 16 and 22 hours (14:00 and 20:00 local time), and those flower aggregates are larger. Sec-

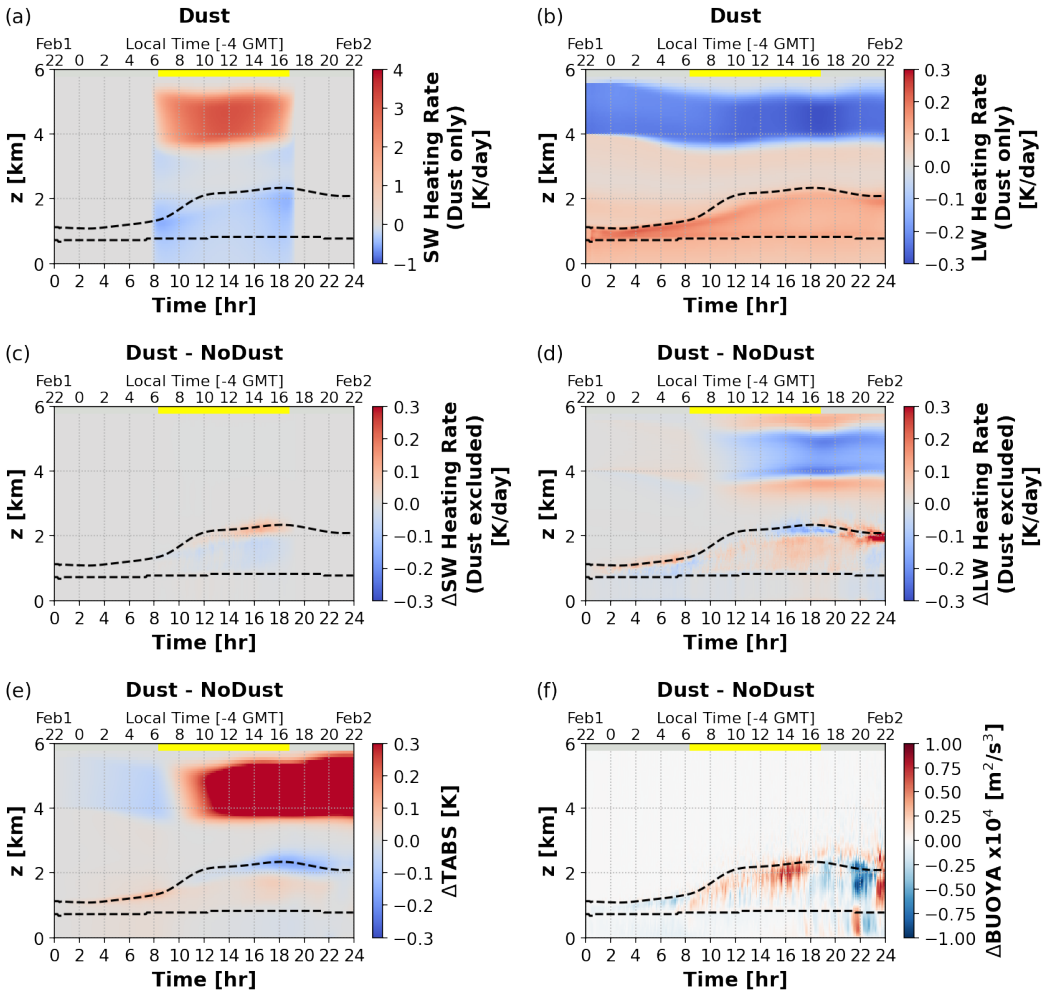

Figure 11. Time-height curtains of the differences between the Dust and NoDust simulations: (a) shortwave radiative heating of the mineral dust, (b) longwave radiative heating of the mineral dust, (c-d) the longwave and shortwave radiative heating rate from the atmosphere excluding the radiative impacts of the mineral dust, (e) the temperature, and (f) the resolved and subgrid-scale buoyant turbulence kinetic energy production (or buoyancy flux).

tion 5.3 will show that this arises from differences in the mesoscale circulation that helps accelerate the transition from sugar to flowers in the non-precipitating shallow cumulus regime.

5.2 The impact of mineral dust on the radiation from a large-scale perspective

Figure 11 shows the radiative heating properties of the mineral dust and their effects on the cloud production, which in turn affects the boundary layer and the cloud system. During the day, the mineral dust absorbs the solar radiation, resulting in weaker boundary-layer shortwave heating (cooling effect of the dust) in the Dust simulation (Fig. 11a). The shortwave contribution of the dust is stronger than the longwave contribution of the dust (Fig. 11b), which heats up the cloud layer during the entire simulation. The shortwave contribution associated with the dust is also stronger than the shortwave heating and longwave cooling associated with the water vapor and cloud water (Fig. 11c-d). Figure 11e-f shows the difference in the temperature and the buoyant turbulence kinetic energy (TKE) production (or buoayncy flux) between the Dust and NoDust simulations, respectively. It shows that before sunrise (hours 0-8), the warming effect of the mineral dust results in a weaker buoyant TKE production, suppressing the sugar formation in the Dust simulation, hence less cloud condensates. After sunrise, the cooling effect of the mineral dust takes effect, resulting in a stronger buoyant TKE production and hence a more vigorous flower formation. More moisture is transported by stronger turbulence in the Dust simulation to the top of the boundary layer. The greater moisture availability and the cooler temperature in the cloud layer result in the accumulation of liquid water, which also cools the top of the boundary layer further. As a result, the Dust simulation produces more clouds in the afternoon (hours 14-18). After sunset (hours 18-24), only the warming effect of mineral dust remains. The TKE production is suppressed, weakening the upward water flux in the Dust simulation and resulting in less cloud and precipitation production compared to the NoDust simulation.

5.3 The impact of mineral dust on local radiation and the mesoscale organization

The rest of this section aims to understand the radiative impact of the mineral dust on the mesoscale organization of the clouds from the local perspective. It is hypothesized that the mineral dust modulates the mesoscale circulation associated with the shallow cumulus plumes through radiation. Figure 12 shows the cross section through two flower aggregates from the Dust simulation at hour 18 of the simulation (20 UTC or 16:00 local time). Figure 12b shows the cross section of the mineral dust concentration (MD).

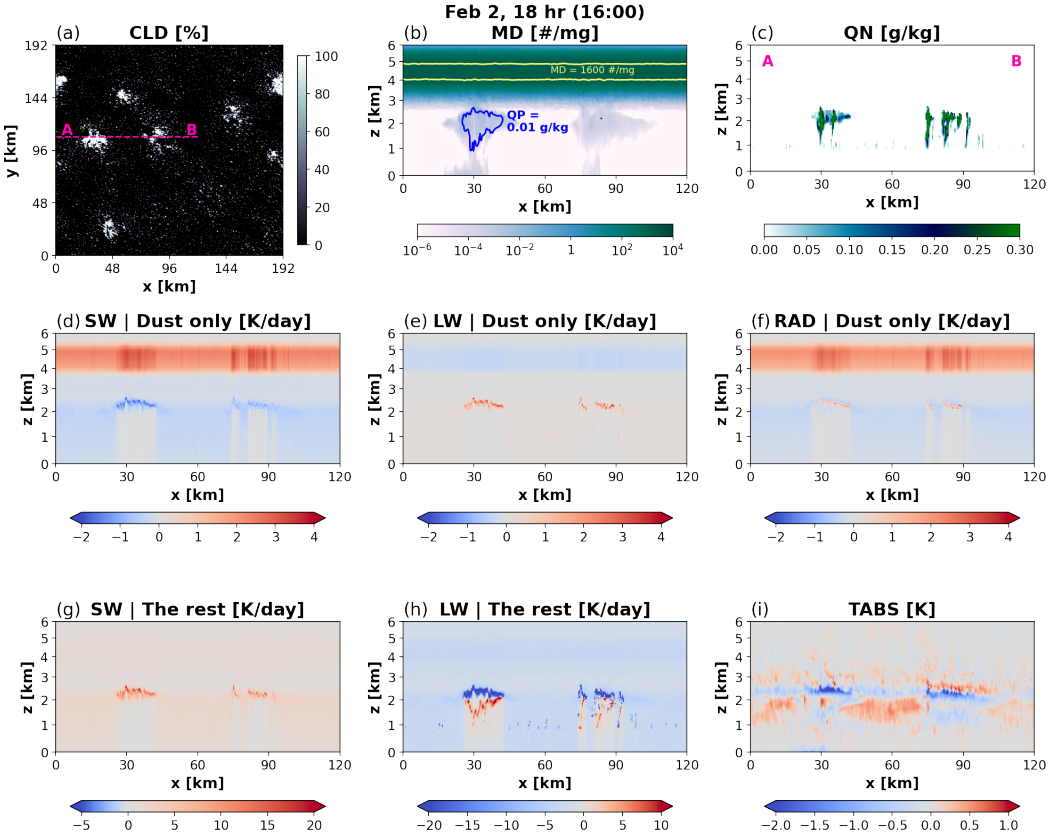

Figure 12. (a) A snapshot of the cloud fraction from the Dust simulation at 20 UTC (hour 18 or 16:00 local time). A cross section is drawn following the dashed pink line through two organizing 'flower' shallow cumuli. The flower on the left is more mature than the flower on the right. (b-c) Cross sections of mineral dust (MD) and cloud water mixing ratio (QN), respectively. In panel (b), a contour of rain water mixing ratio (QP) of 0.01 g/kg is shown in blue. The light yellow lines near the top of the panel indicate the levels of high mineral dust concentrations (1600 mg^{-1} or greater). (d-f) Cross sections of shortwave, longwave, and total radiative heating rates from only the mineral dust in the Dust simulation. (g-h) Shortwave and longwave radiative heating rates from everything else except for the mineral dust in the Dust simulation. (i) The temperature anomalies from the domain average at the cross section.

By this time, a small amount of mineral dust is entrained into the boundary layer inside the cloud plumes, shown by the light blue shading. The precipitating downdrafts further assist in bringing the mineral dust to the surface.

The mineral dust in the free troposphere (and some that is entrained into the cloud plumes) result in extra shortwave cooling and longwave heating at the top of the clouds (Fig. 12d-f). The change in radiative heating results in a change of buoyant TKE production as the air above the cloud plume is destabilized, allowing more vigorous cloud formation. Figure 12g-h shows the shortwave and longwave radiative heating rates due to the rest of the atmospheric components except the mineral dust. The extra total water in the cloud plumes contributes to extra shortwave heating and (a much stronger) longwave cooling. Overall, there is a negative temperature anomaly at the top of the cumulus clouds compared to the surrounding regions (Fig. 12i). This helps destabilize the air inside the cloud plumes, promoting more vigorous cloud turbulence and higher cloud fraction.

That the air inside flower clouds is cooler than the surrounding regions is true at all times and consistent in both NoDust and Dust simulations. Figure 13a shows the temperature perturbations (T'') binned by the TWP quartiles of both simulations at 20 UTC (16:00). The moistest TWP quartile (Q4) represents areas with the flower aggregates, whereas the driest TWP quartile (Q1) represents the cloud-free regions. At a later time, when the flower clusters are larger, the cooling anomaly in the moistest TWP quartile (T'' from Q4) is almost -1 K in the Dust simulation (Fig. 13b). During the times when the Dust simulation produces more clouds than NoDust, T'' from Q4 of the Dust simulation is also more negative (Fig. 13c, until hour 18). This implies that a rising air parcel inside the clouds from the Dust simulation will gain more buoyancy as it encounters the cooler air. This condition is favorable for stronger upward motions inside the cloud plumes leading to stronger lower-level moisture convergence in the moist regions, as shown in similar plots of the vertical velocity purterbations (w'') (Fig. 13d-f) and the mesoscale convergence of total water ($\mathcal{C}$) (Fig. 13g-i). The w'' and $\mathcal{C}$ profiles are more positive in Q4 of the Dust simulation during the times when the Dust simulation produces more clouds (Fig. 13f, i).

The differences in T'', w'', and $\mathcal{C}$ between the Dust and NoDust simulations are negative at night (hours 18-22 in the right column of Figure 13). During this time, the ex-

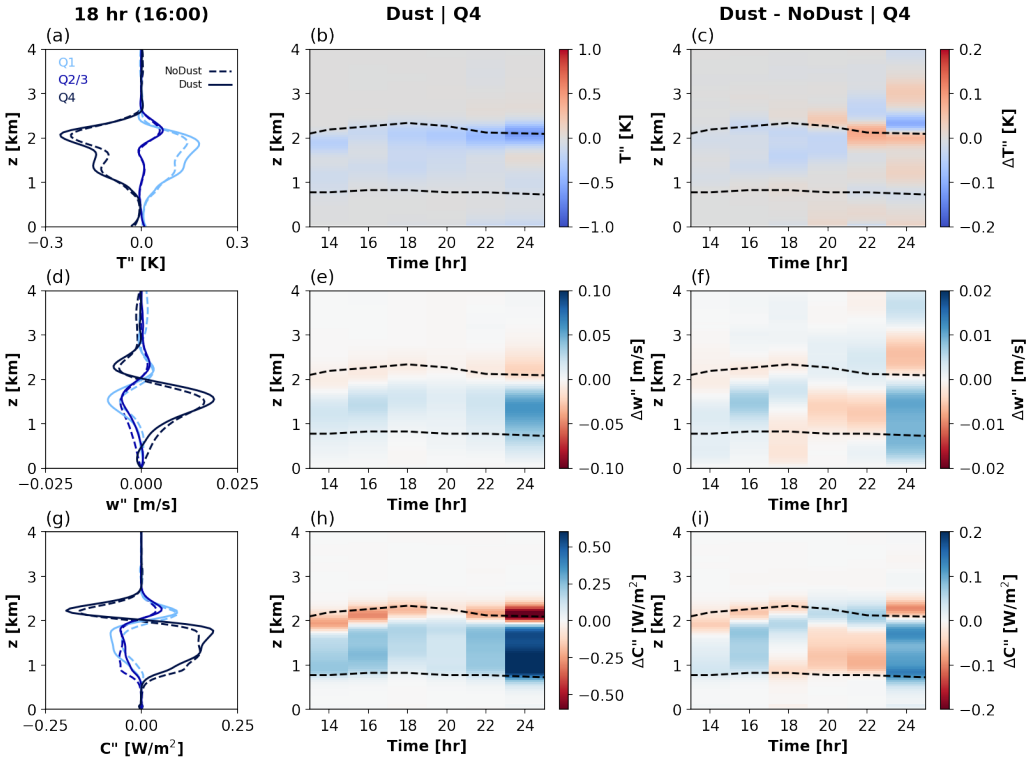

Figure 13. (a) Vertical profiles of the mesoscale temperature perturbations (T'') at 20 UTC (hour 18 or 16:00 local time, same as in Figure 12) binned by TWP quartiles. (b) Time-height curtains of T'' averaged over the highest TWP quartile or Q4 from the Dust simulation at 16 UTC to 2 UTC (hours 14 through 24). (c) Time-height curtains of the differences in T'' of Q4 between the Dust and NoDust simulations at hours 14 through 24. (d-f) As in Panels (a-c) but for the mesoscale vertical velocity perturbations (w''). (g-i) As in Panels (a-c) but for the mesoscale convergence of total water ($\mathcal{C}$).

tra longwave heating due to the entrained mineral dust inside the cloud plumes helps to stabilize the cloud layer, weakening the mesoscale upward motion (less positive w'' in Q4) and the mesoscale convergence of total water to the moist areas (less positive $\mathcal{C}$). Therefore, the mesoscale organization is weaker in the Dust simulation after sunset. At hour 24, the mesoscale circulation in the Dust simulation is strengthened again. At this point, more mineral dust is entrained into the boundary layer but it is not removed by sedimentation in the simulation since it is only allowed to interact with the radiation scheme. An accurate representation of this state requires coupling the mineral dust with the cloud microphysics scheme and is beyond the scope of this paper, which focuses on the aerosol-radiation interaction and its impacts on the clouds.

Figure 14 summarizes the above findings by presenting time series of two organization diagnostics, and the ratio of the buoyant TKE production and total water spectra between Dust and NoDust. They consistently show that the Dust simulation has stronger organization rate during the end of the day (larger mean area of cloud aggregates and greater normalized TWP standard deviation, Fig. 14a-b). The cloud-layer TKE production spectra and the boundary-layer QT spectra in the mesoscale of the Dust simulation increase with the organization diagnostics (Fig. 14c-d). The TKE production and QT spectral ratios between the Dust and NoDust simulations associated with wavelengths greater than 4 km and smaller than 48 km are greater than 1 between hours 8 and 20 (Fig. 14e-f). They suggest that during this period, the boundary-layer total water (vapor, cloud water, and rain) is more aggregated in the mesoscale in the Dust than NoDust simulations because of the stronger TKE production inside the clouds. This is in agreement with a larger $\mathcal{C}$ term in the moistest quartile of the Dust simulation (Fig. 13i), and consistent with the findings by Narenpitak et al. (2021). The mechanism responsible for the transition from sugar to flower shallow cumuli that do not precipitate heavily is still the mesoscale circulation that leads to net convergence of moisture in the already moist and cloudy regions. The mesoscale circulation is strengthened further during the day when mineral dust is present above the cloud layer, because the free-tropospheric mineral dust absorbs the shortwave radiation and results in extra radiative cooling in the boundary layer.

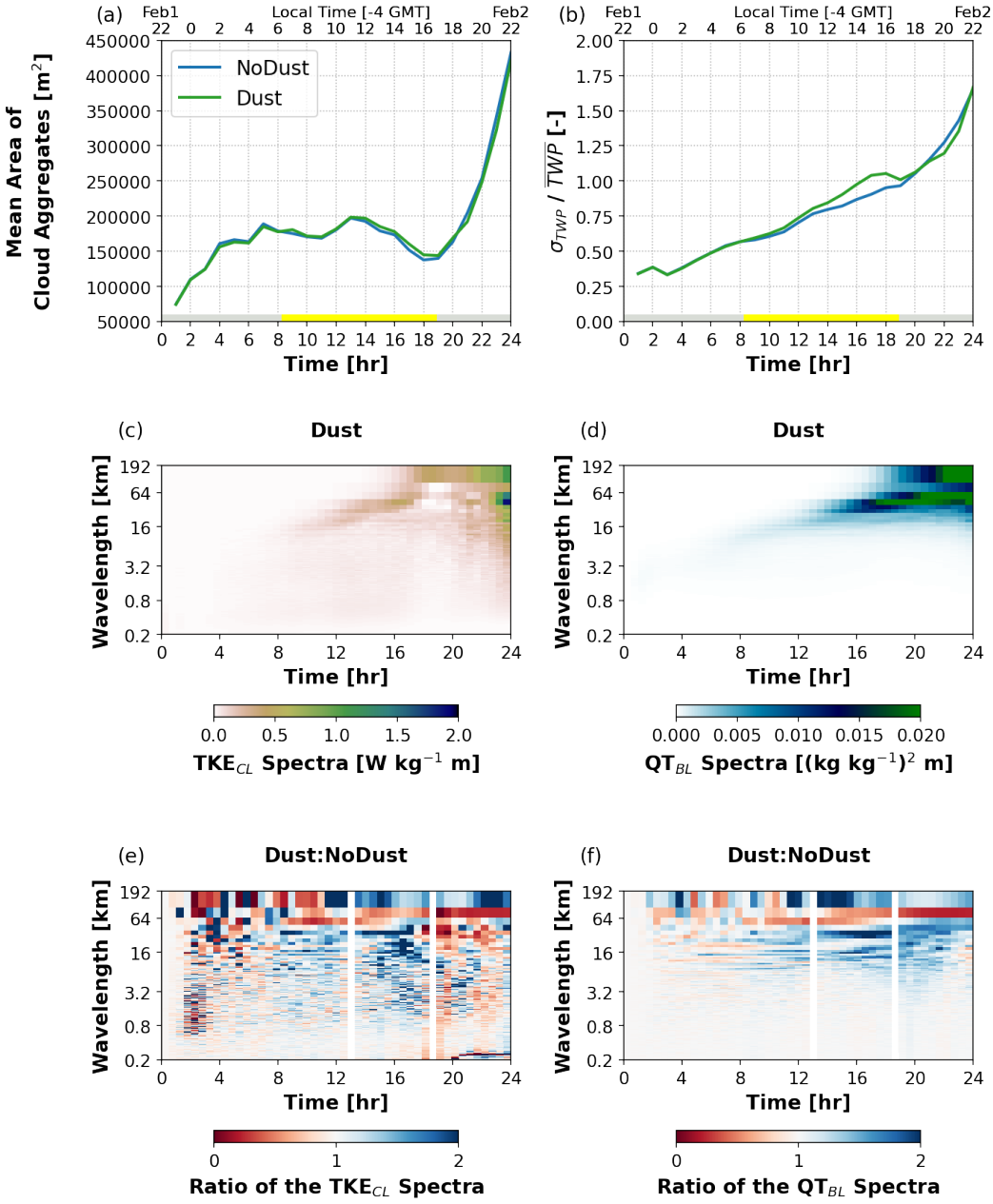

Figure 14. Organization diagnostics from the NoDust and Dust simulations: (a) the mean area of cloud aggregates and (b) the normalized TWP standard deviation. (c) The hourly spectra of the cloud-layer buoyant turbulence kinetic energy (TKE$_{CL}$) production from the Dust simulation. (d) The hourly spectra of the boundary-layer total water mixing ratio (QT$_{BL}$) from the Dust simulation. (e) Ratios of the TKE$_{CL}$ spectra between the Dust and NoDust simulations. (f) Ratios of the QT$_{BL}$ spectra between the Dust and NoDust simulations.

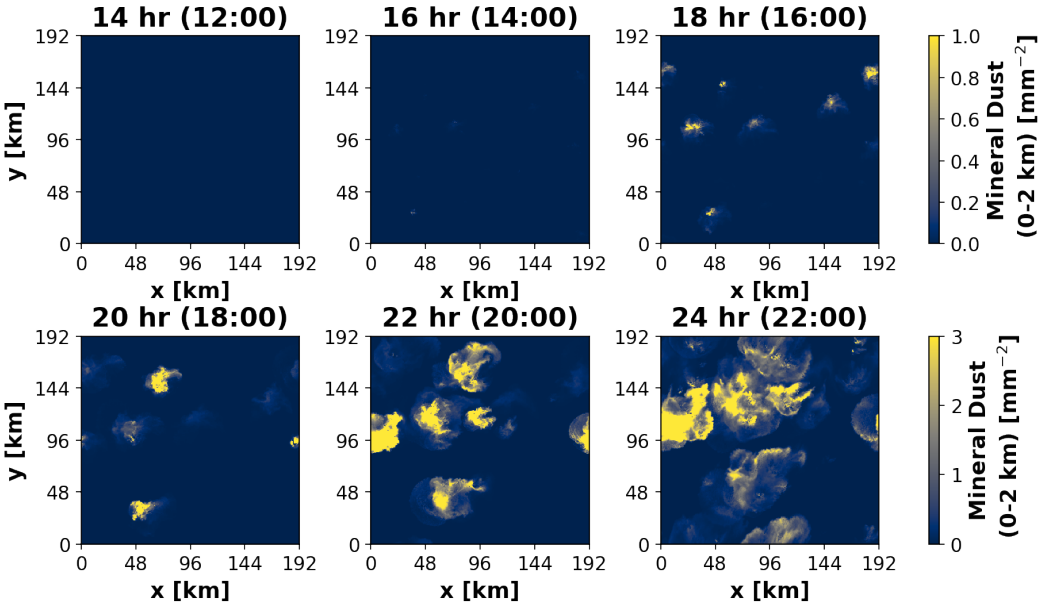

Figure 15. Snapshots of the mineral dust number concentration integrated within the lower 2 km of the Dust simulations, plotted every 2 hours from hours 14 through 24.

5.4 Mineral dust as a tracer

In the Dust simulation, the mineral dust not only alters the heating and moisture budgets of the cloud layer, but it also acts as an atmospheric tracer. Initialized above the shallow cumulus layer, the mineral dust is advected in all directions as the simulation progresses. A small amount of mineral dust diffuses into the inversion layer above the flower cloud aggregates. The local descending air in the inversion layer above the clouds brings the mineral dust inside the flower aggregates (e.g., Fig. 15 at hour 18). At this state, the mineral dust is entrained into the boundary layer by the mesoscale circulation associated with the clouds. The precipitating downdrafts bring the mineral dust down further, and the surface divergence below the cloud aggregates helps spread the the mineral dust farther, but it is still contained within the edges of the cold pools.

6 Conclusions

The ATOMIC/EUREC^{4}A field campaign took place in January-February 2020 over the Atlantic Ocean east of Barbados. One of its goals is to advance the understanding of shallow cumulus clouds, mesoscale processes, circulation, and their interactions with

the weather and climate. On February 2, 2020, a shallow cumulus transition from sugar to flower clouds was observed. The event was simulated using a Lagrangian large eddy simulation following an airmass trajectory along the trade winds for 24 hours. The cloud depth and cloud liquid water increase along the trajectory with large-scale upward vertical motion. As the transition from the sugar cloud state to the flower cloud state takes place, cloud aggregation and mesoscale organization become stronger. Net convergence of moisture associated with mesoscale circulation renders the moist areas moister, strengthening the organization and supports the cloud transition.

The observed sugar-to-flower transition occurred during the day and produced light precipitation and cold pools at night. This event is captured in the control simulation. A sensitivity simulation is performed with the same large-scale forcings except with a delay in the insolation by 12 hours, leading to a sugar-to-flower transition event that occurs at night. The clouds grow deeper around the same time as in the control simulation, when the large-scale vertical motions are positive, but the cloud and rain amounts reach their maximum values 10-12 hours sooner. The Nighttime-transition simulation proves that the cloud amount and cloud depth are sensitive to the timing of the diurnal cycle. Not only are the flower clouds in the Nighttime simulation much thicker, but they also are more strongly organized, having larger cloud aggregate areas and fewer aggregate counts.

Having transitioned at night, the flower aggregates in the Nighttime simulation also produce stronger precipitation, with more abundant and stronger cold pools, as measured by the buoyancy proxy and the surface divergence. The near-surface divergence associated with the precipitating downdrafts creates strong gust fronts at night, shifting the moisture from the moist, cloudy columns to drier surrounding regions. This encourages a new generation of convection to form along the edges of the cold pools. Each cloud and cold pool interaction cycle lasts a few hours, and there are a few cycles of such interactions throughout the night. The cloud and rain amount decrease as the sun rises. The cloud and cold pool processes described above take place in the flower aggregates formed at night in our simulation, but not in those formed during the day. They also dominate the original mechanism that is responsible for the mesoscale organization in the control simulation when considered in a scale larger than the diameter of the cold pools.

During the field campaign, the observed sugar-to-flower transition occurred under a layer of mineral dust in the free troposphere, and we study whether the interaction of the mineral dust with radiation affects the mesoscale organization of the clouds. It is found that the simulation with free-tropospheric mineral dust produces a slightly more rapid transition, higher cloud liquid water, and stronger organization during the day. This is because the mineral dust absorbs the shortwave radiation and cools the boundary layer below. This allows a more vigorous mesoscale circulation that supports the original mechanism whereby the moist areas become moister and dry areas become drier, accelerating the sugar-to-flower transition. However, at night the mineral dust and extra cloud water result in longwave heating that weakens the mesoscale circulation, slightly reducing cloud water.

Overall, both the diurnal cycle and the free-tropospheric mineral dust have impacts on the radiation, but the 12-hour delay in the diurnal cycle has a much stronger radiative effect than the mineral dust. With the diurnal cycle shift, the shortwave radiation is completely removed ($\sim \mathcal{O}(1000\ \mathrm{W\ m^{-2}})$), while the longwave radiation remains the same. On the other hand, the free-tropospheric mineral dust results in a 65 W $\mathrm{m^{-2}}$ reduction in the shortwave radiation and a slight change in the longwave radiation, both in the day and the night. Therefore, the timing of the diurnal cycle is more important than the mineral dust and leads to a more significant change in the cloud system in multiple ways, i.e., greater cloud amount, deeper cloud layer, larger and fewer flower cloud aggregates, stronger precipitation, and stronger cold pools. The deeper and stronger cold pools further alter the dynamics of the cloud system, causing new shallow convection to form at the edge of the cold pools, which are in the relatively drier regions. On the other hand, the free-tropospheric mineral dust results in a slight increase in the cloud amount because of a stronger cloud organization during the day. However, this change does not alter the main mechanism that promotes the organization and the transition of the clouds.

The Dust simulation shows that the mineral dust is entrained into the cloud aggregates and the mixed layer via air motions around and inside the shallow cumulus plumes. In reality, the dust particles could also act as cloud condensation nuclei that might lead to a stronger buildup of liquid water and stronger drizzle. These may alter the cloud and cold pool interaction further. Additional simulations that allow the mineral dust to interact with both the radiative and cloud microphysics schemes will shed light on this. The sensitivity of the sugar-to-flower transition to atmospheric radiation raises the in-

teresting question of its response to anthropogenic climate change, which involves a warmer ocean, atmosphere, and higher greenhouse gas concentrations, all of which change atmospheric radiation. This warrants further investigation of the sugar-to-flower transition.

Appendix A The surface fluxes from the Daytime and Nighttime simulations

Previous studies found that at night, shallow cumulus clouds have greater cloud fraction and are deeper than during the day. Often, they have stronger surface wind speed at night, leading to stronger latent heat flux (LHF), deeper cloud layer, stronger mixing, and weaker sensible heat flux (SHF), which can promote the cloud formation further (Nuijens & Stevens, 2012; Vial et al., 2021). In this case, the surface wind speed are the same between Daytime and Nighttime simulations. In both simulations, the LHF and SHF tendencies follow that of the surface wind speed (Fig. A1). The Nighttime simulation has weaker LHF and SHF than the Daytime simulation during the first 12 hours. This is as expected, because it is daytime in the first five hours of the Nighttime simulation; the shortwave heating warms the boundary layer and the SHF does not need to be as strong. The LHF is initially smaller as the Nighttime simulation initially produces less cloud water than the Daytime simulation. In the second half, the Nighttime simulation produces stronger LHF and SHF than Daytime, and hence stronger Bowen ratio.

Appendix B The total water perturbation budget

The budget of mesoscale total water perturbations ($q_t''(x_m, y_m, z, t)$) can be described as:

$$\frac{\partial q_t''}{\partial t} = \mathcal{A} + \mathcal{F} + \mathcal{C} + \mathcal{S} \quad . \tag{B1}$$

Each term on the right hand side of Equation B1 is as follows: The first term is the advection of mesoscale variability due to the trajectory-relative large-scale wind ($\overline{\boldsymbol{v}}(z,t)$) and the mesoscale perturbations of the wind velocity ($\boldsymbol{v}''(x_m, y_m, z, t)$) in both the horizontal and vertical directions:

$$\mathcal{A} = -(\overline{\boldsymbol{v}} + \boldsymbol{v}'') \cdot \nabla q_t'' \quad . \tag{B2}$$

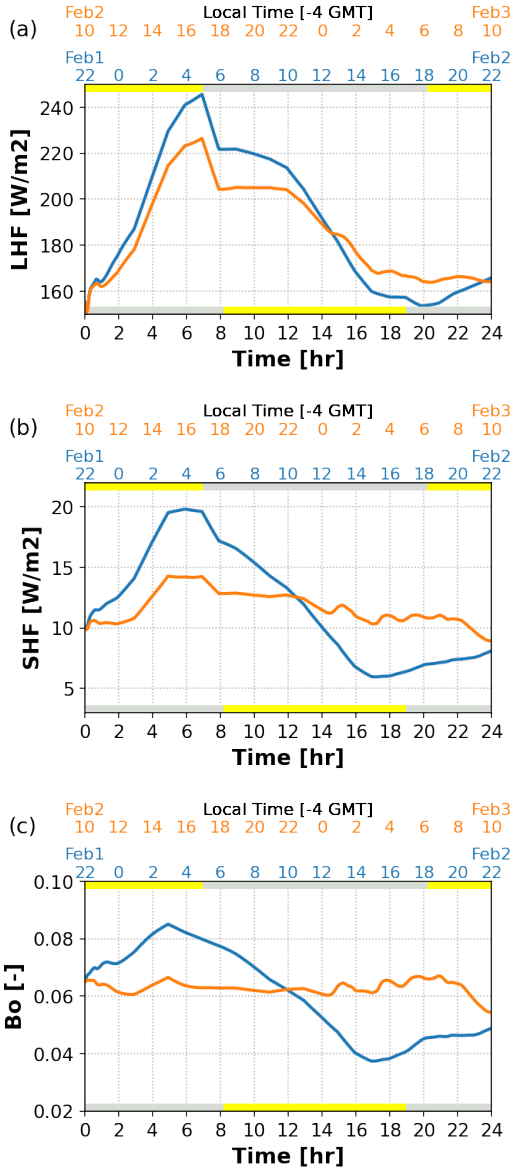

Figure A1. As in Figure 1 but for the surface latent heat flux (LHF), surface sensible heat flux (SHF), and the Bowen ratio (Bo = SHF/LHF) from the Daytime and Nighttime simulations.

Let $[\quad]''$ denote coarse-graining of the cumulus-scale field inside the brackets to a mesoscale region of 16×16 km^2, and let ρ denote the reference density profile. The second term represents the vertical and horizontal gradients of the cumulus-scale q_t flux ($\boldsymbol{v}'''q_t'''$) coarse-grained to 16×16 km^2:

$$\mathcal{F} = -\frac{1}{\rho}\nabla \cdot [\rho \boldsymbol{v}'''q_t''']'' \quad . \tag{B3}$$

Eq. (B3) was derived with the anelastic approximation used in SAM. $\mathcal{F}$ could also be referred to as the total water transport by thermals in cumulus scales.

The third term is the mesoscale vertical advection of large-scale q_t ($\overline{q_t}(z,t)$):

$$\mathcal{C} = -w''\frac{\partial \overline{q_t}}{\partial z} \quad . \tag{B4}$$

As described in the main text, because $\frac{\partial \overline{q_t}}{\partial z}$ is always negative in the shallow cumulus layer, the signs of $\mathcal{C}$ follow the signs of w'', which imply local convergence and divergence based on the mass continuity equation. Thus, a positive $\mathcal{C}$ physically means there is a convergence of the total water into the considered mesoscale tile.

Finally, the fourth term is the source term of q_t'', which represents the mesoscale perturbations of the precipitation mass flux (F_p) divergence:

$$\mathcal{S} = -\frac{1}{\rho}\left[\frac{\partial F_p}{\partial z}\right]'' \quad . \tag{B5}$$

In a heavily-precipitating shallow cumulus deck, the mesoscale perturbations of the precipitation mass flux divergence or $\mathcal{S}$ is nontrivial. A full derivation of the q_t'' budget can be found in Appendix D of Narenpitak et al. (2021).

These four terms from the Daytime-transition simulation (also known as NoDust simulation), Nighttime-transition simulation, and the Dust simulation are shown in Figures B1-B3, respectively.

Figures 6 and B2 show that between hours 16 and 20, when the Nighttime simulation produces a lot of cold pools, the $\mathcal{C}$ term is negative in the subcloud layer of the highest TWP quartile (Q4) when using the 16-km mesoscale tile size. Figure B4d-f shows that when smaller tile sizes are used (6.4 km or smaller), $\mathcal{C} > 0$ everywhere in the cloud layer of Q4, meaning that there is still net moisture convergence in the moist columns associated with the clouds despite the moisture divergence near the surface. The near-surface mesoscale moisture divergence is associated with the gust fronts of the cold pools.

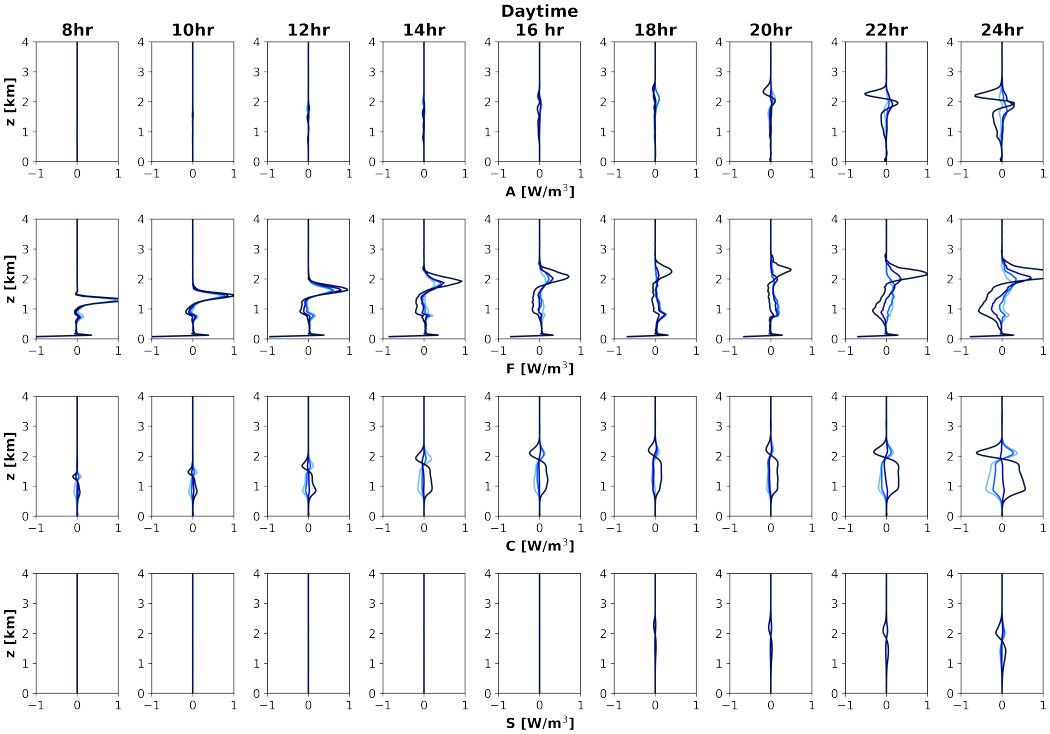

Figure B1. Vertical profiles showing the four main terms in the budget of mesoscale total water perturbations (q_t'') from the Control simulation: (top row) The advection of mesoscale q_t variability due to the large-scale and mesoscale winds in both the horizontal and vertical directions ($\mathcal{A}$), (second row) the vertical and horizontal gradients of the cumulus-scale q_t flux coarse-grained to a mesoscale tile also in both the horizontal and vertical directions ($\mathcal{F}$), (third row) the mesoscale vertical advection of large-scale q_t or the mesoscale convergence of total water ($\mathcal{C}$), and (bottom row) the mesoscale perturbations of the precipitation mass flux divergence ($\mathcal{S}$). All of these profiles are computed for the 16-km tile size and binned by the TWP quartiles, from Q1 representing the driest regions (light blue) to Q4 representing the moistest regions (dark blue). The profiles are shown every two hours from hours 8 (left) to 24 (right).

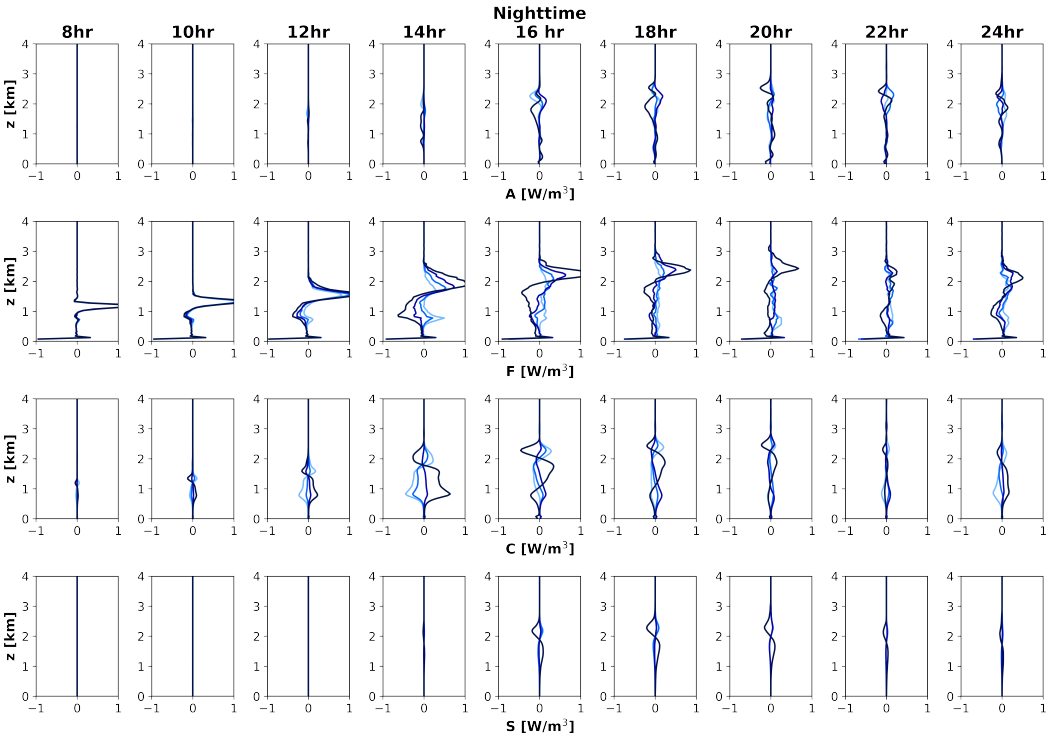

Figure B2. As in Figure B1 but for the Nighttime-transition simulation.

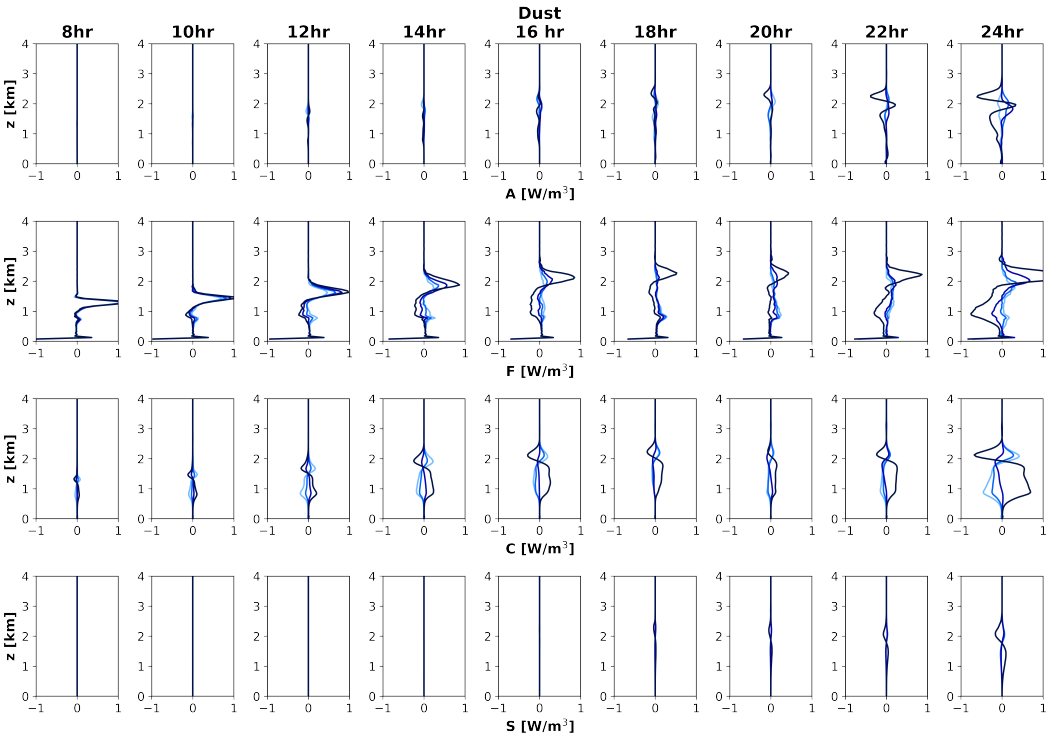

Figure B3. As in Figure B1 but for the Dust simulation.

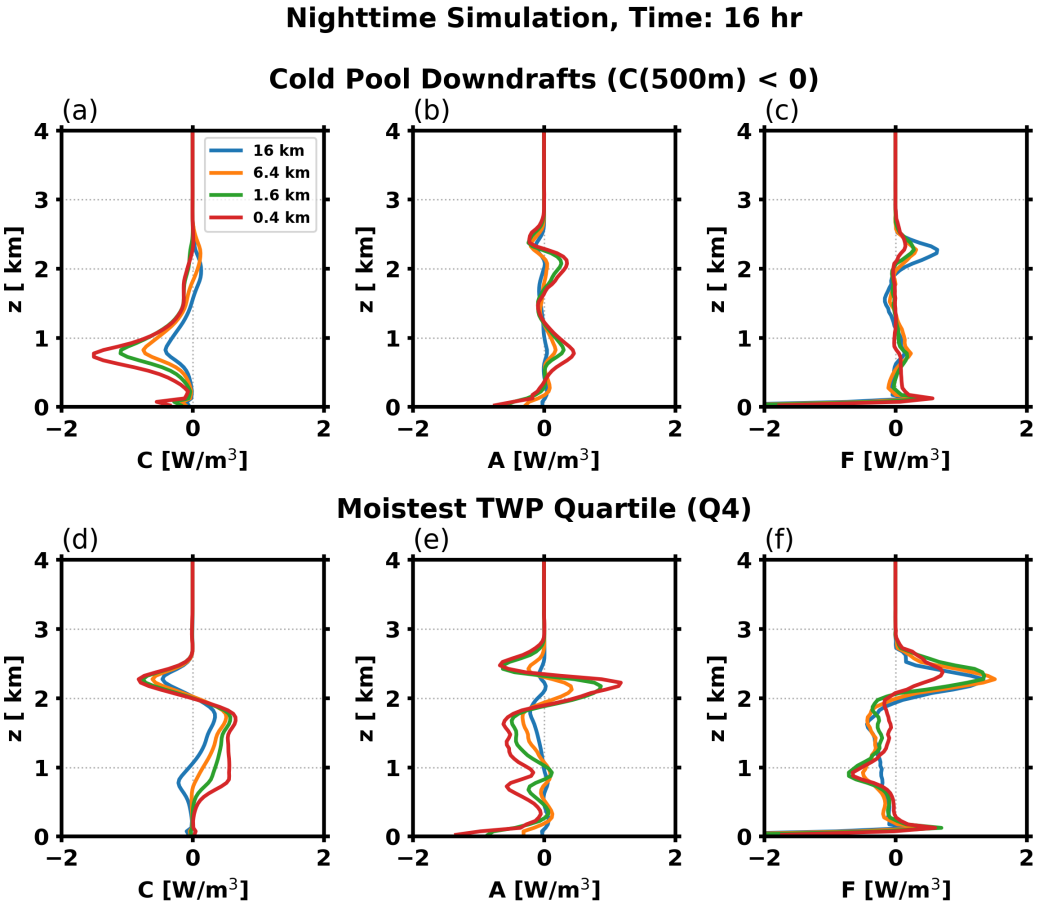

Figure B4. Profiles of the first three terms on the right hand side of Equation B1 – $\mathcal{C}$, $\mathcal{A}$, and $\mathcal{F}$ – computed using multiple tile sizes for the Nighttime simulation at hour 16, when the cold pools are abundant and strong. (a) The $\mathcal{C}$ term composited from the vertical columns in which $\mathcal{C}$ is negative at 500 m (i.e., where there is mesoscale divergence of total water near the surface). (b-c) The $\mathcal{A}$ and $\mathcal{F}$ terms composited from the same vertical columns as in panel (a), showing that the mesoscale divergence of total water in the mixed layer is compensated by the upward mesoscale total water advection and upward vertical total water transport by mixed layer thermal. Although both the horizontal and vertical components of the $\mathcal{A}$ and $\mathcal{F}$ terms are included, the horizontal contributions are small. (d-f) The $\mathcal{C}$, $\mathcal{A}$, and $\mathcal{F}$ profiles averaged within the moistest TWP quartile or Q4 of the Nighttime simulation.

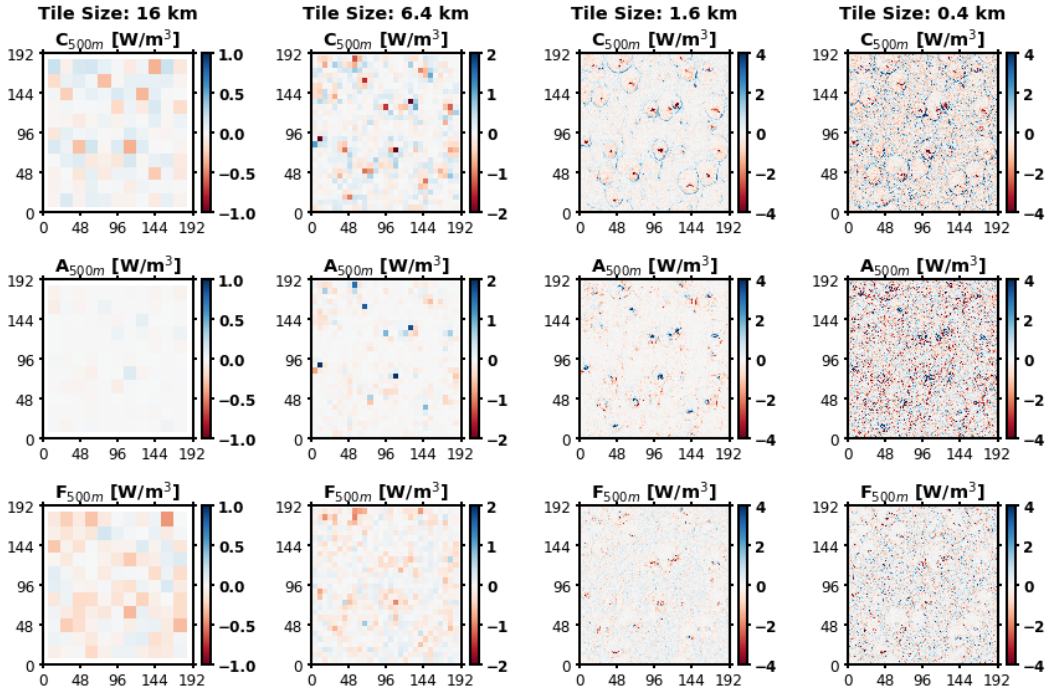

Figure B5. Snapshots of the (top) $\mathcal{C}$, (middle) $\mathcal{A}$, and (bottom) $\mathcal{F}$ terms at 500 m altitude from the Nighttime simulation at hour 16. The terms are computed at various tile sizes: 16 km, 6.4 km, 1.6 km, and 0.4 km. Note the different scales of the color bars for different tile sizes

Sufficiently high resolution is needed to examine this process. This is demonstrated further in Figure B5 and summarized in B4a-c.

Figure B5 shows that inside the precipitating downdrafts, there is local divergence of total water ($\mathcal{C} < 0$) in the mixed layer (approximately lower 1 km of the atmosphere), and local convergence of total water ($\mathcal{C} > 0$) at the edges of the cold pools. These follow the signs of the surface divergence and convergence (w'' near the surface), which are the characteristics of the cold pools. The middle row shows that where $\mathcal{C} < 0$, there is upward advection of the mesoscale total water perturbations ($\mathcal{A} > 0$). Both the horizontal and vertical contributions are shown in the snapshots, but the horizontal contributions are small. The vertical contributions of $\mathcal{A}$ are washed out when computed using larger mesoscale tile sizes. However, the surface divergence remains strong even with larger mesoscale tile sizes as long as the tile sizes are smaller than the horizontal extents of the cold pools. The cumulus-scale fluxes or $\mathcal{F}$ are smaller than the other two terms.

This is summarized by the composite profiles of $\mathcal{C}$ and $\mathcal{A}$ in the columns where $\mathcal{C} < 0$ at 500 m. This represents all of the precipitating downdrafts as well as some other drier and cloud-free regions. Still, the $\mathcal{A}$ composite profiles are still positive in this level, suggesting that the total water divergence ($\mathcal{C} < 0$) is still being compensated by the vertical advection of the total water perturbations ($\mathcal{A} > 0$). This is also in agreement with the known cloud and cold pool dynamics that as the downdrafts diverge at the surface, the gust fronts carry the extra moisture to the areas that are once cloud-free and encourage new cycle of convection through lifting of the moist air (Zuidema et al., 2012). In general, this shows that the total water convergence ($\mathcal{C} > 0$ still takes place in the mixed layer of the moist regions, as in the control simulation. However, with the cold pool dynamics, the total water convergence takes place over a smaller scale in the mixed layer.

Acknowledgments

This study was supported by NOAA's Climate Program Office, Climate Variability and Predictability Program (GC19-303). The PMEL contribution number is 5383. The authors thank scientists, technicians, pilots, crew members, and everybody who made the ATOMIC and EUREC^{4}A field campaign possible. We thank Marat Khairoutdinov, Stony Brook University, for providing the System for Atmospheric Modeling (SAM). We thank Pierre Coutris, French National Centre for Scientific Research (CNRS), for providing data from the Ultra-High-Sensitivity Aerosol Spectrometer (UHSAS) and the Cloud Droplet Probe (CDP-2) on the French ATR-42 research aircraft. We acknowledge the NOAA Research and Development High Performance Computing Program for providing computing and storage resources that have contributed to the research results reported within this paper. ERA5 data were generated using Copernicus Climate Change Service Information. Neither the European Commission or ECMWF is responsible for any use that may be made of the Copernicus information or data in this publication.The WACCM-CESM1 CMIP5 outputs were retrieved from the Centre for Environmental Data Analysis (CEDA) archive, and the available ensemble members were r2i1p1, r3i1p1, and r4i1p1 from the RCP 8.5 simulations. Simulation outputs from this study are available at `https://csl.noaa.gov/groups/csl9/datasets/data/cloud_phys/`.

References

Albrecht, B., Ghate, V., Mohrmann, J., Wood, R., Zuidema, P., Bretherton, C.,

... Schmidt, S. (2019). Cloud system evolution in the trades (cset): Following the evolution of boundary layer cloud systems with the nsf–ncar gv. *Bulletin of the American Meteorological Society*, *100*(1), 93 - 121. doi: 10.1175/BAMS-D-17-0180.1

Andrews, T., Gregory, J. M., Webb, M. J., & Taylor, K. E. (2012). Forcing, feedbacks and climate sensitivity in cmip5 coupled atmosphere-ocean climate models. *Geophysical Research Letters*, *39*(9), L09712. Retrieved from `https://agupubs.onlinelibrary.wiley.com/doi/abs/10.1029/2012GL051607` doi: https://doi.org/10.1029/2012GL051607

Blossey, P. N., Bretherton, C. S., Zhang, M., Cheng, A., Endo, S., Heus, T., ... Xu, K. M. (2013). Marine low cloud sensitivity to an idealized climate change: The CGILS LES intercomparison. *Journal of Advances in Modeling Earth Systems*, *5*(2), 234–258. doi: 10.1002/jame.20025

Bony, S., & Dufresne, J. L. (2005). Marine boundary layer clouds at the heart of tropical cloud feedback uncertainties in climate models. *Geophysical Research Letters*, *32*(20), 1–4. doi: 10.1029/2005GL023851

Bony, S., Lothon, M., Delanoë, J., Coutris, P., Etienne, J.-C., Aemisegger, F., ... Vogel, R. (2022). EUREC^{4}A observations from the SAFIRE ATR42 aircraft. *Earth System Science Data Discussions*, *2022*, 1–61. doi: 10.5194/essd-2021-459

Bony, S., Schulz, H., Vial, J., & Stevens, B. (2020). Sugar, gravel, fish, and flowers: Dependence of mesoscale patterns of trade-wind clouds on environmental conditions. *Geophysical Research Letters*, *47*(7), 1–9. doi: 10.1029/2019gl085988

Bony, S., Stevens, B., Ament, F., Bigorre, S., Chazette, P., Crewell, S., ... Wirth, M. (2017). EUREC4A: A field campaign to elucidate the couplings between clouds, convection and circulation. *Surveys in Geophysics*, *38*(6), 1529-1568. doi: https://doi.org/10.1007/s10712-017-9428-0

Boucher, O., Randall, D., Artaxo, P., Bretherton, C., Feingold, G., Forster, P., ... Zhang, X. Y. (2013). Clouds and aerosols. In *Climate change 2013 the physical science basis: Working group i contribution to the fifth assessment report of the intergovernmental panel on climate change.* doi: 10.1017/CBO9781107415324.016

Bretherton, C. S., & Blossey, P. N. (2017). Understanding mesoscale aggregation of

shallow cumulus convection using large-eddy simulation. *Journal of Advances in Modeling Earth Systems*, *9*(8), 2798–2821. doi: 10.1002/2017MS000981

Bretherton, C. S., Blossey, P. N., & Jones, C. R. (2013). Mechanisms of marine low cloud sensitivity to idealized climate perturbations: A single-LES exploration extending the CGILS cases. *Journal of Advances in Modeling Earth Systems*, *5*(2), 316–337. doi: 10.1002/jame.20019

Coutris, P., & Ehses, G. (2021). *SAFIRE ATR42: UHSAS dataset.* doi: https://doi.org/10.25326/220

d'Almeida, G. A., Koepke, P., & Shettle, E. P. (1991). *Atmospheric aerosols: Global climatology and radiative characteristics.* Hampton, Va.: A. Deepak Pub.

Feingold, G., Walko, R. L., Stevens, B., & Cotton, W. R. (1998). Simulations of marine stratocumulus using a new microphysical parameterization scheme. *Atmospheric Research*, *47–48*, 505–528. doi: 10.1016/S0169-8095(98)00058-1

Gutleben, M., Groß, S., Wirth, M., Emde, C., & Mayer, B. (2019). Impacts of Water Vapor on Saharan Air Layer Radiative Heating. *Geophysical Research Letters*, *46*(24), 14854–14862. doi: 10.1029/2019GL085344

Hersbach, H., Bell, B., Berrisford, P., Hirahara, S., Horányi, A., Muñoz-Sabater, J., ... Thépaut, J.-N. (2020). The ERA5 global reanalysis. *Quarterly Journal of the Royal Meteorological Society*, *146*(730), 1999-2049. doi: https://doi.org/10.1002/qj.3803

Hurrell, J. W., Holland, M. M., Gent, P. R., Ghan, S., Kay, J. E., Kushner, P. J., ... Marshall, S. (2013). The Community Earth System Model: A Framework for Collaborative Research. *Bulletin of the American Meteorological Society*, *94*(9), 1339 - 1360. Retrieved from `https://journals.ametsoc.org/view/journals/bams/94/9/bams-d-12-00121.1.xml` doi: 10.1175/BAMS-D-12-00121.1

Kazil, J., Christensen, M. W., Abel, S. J., Yamaguchi, T., & Feingold, G. (2021). Realism of lagrangian large eddy simulations driven by reanalysis meteorology: Tracking a pocket of open cells under a biomass burning aerosol layer. *Journal of Advances in Modeling Earth Systems*, *13*(12), e2021MS002664. Retrieved from `https://agupubs.onlinelibrary.wiley.com/doi/abs/10.1029/2021MS002664` doi: https://doi.org/10.1029/2021MS002664

Khairoutdinov, M. F., & Randall, D. A. (2003). Cloud Resolving Modeling of

the ARM Summer 1997 IOP: Model Formulation, Results, Uncertainties, and Sensitivities. *Journal of the Atmospheric Sciences*, *60*(4), 607–625. doi: 10.1175/1520-0469(2003)060⟨0607:CRMOTA⟩2.0.CO;2

Marsh, D. R., Mills, M. J., Kinnison, D. E., Lamarque, J.-F., Calvo, N., & Polvani, L. M. (2013). Climate Change from 1850 to 2005 Simulated in CESM1(WACCM). *Journal of Climate*, *26*(19), 7372 - 7391. Retrieved from `https://journals.ametsoc.org/view/journals/clim/26/19/jcli-d-12-00558.1.xml` doi: 10.1175/JCLI-D-12-00558.1

Medeiros, B., Stevens, B., Held, I. M., Zhao, M., Williamson, D. L., Olson, J. G., & Bretherton, C. S. (2008). Aquaplanets, climate sensitivity, and low clouds. *Journal of Climate*, *21*(19), 4974 - 4991. doi: 10.1175/2008JCLI1995.1

Mlawer, E. J., Taubman, S. J., Brown, P. D., Iacono, M. J., & Clough, S. A. (1997). Radiative transfer for inhomogeneous atmospheres: RRTM, a validated correlated-k model for the longwave. *Journal of Geophysical Research: Atmospheres*, *102*(D14), 16663-16682. doi: 10.1029/97JD00237

Narenpitak, P., & Bretherton, C. S. (2019). Understanding negative subtropical shallow cumulus cloud feedbacks in a near-global aquaplanet model using limited area cloud-resolving simulations. *Journal of Advances in Modeling Earth Systems*, *11*(6), 1600–1626. doi: 10.1029/2018MS001572

Narenpitak, P., Kazil, J., Yamaguchi, T., Quinn, P., & Feingold, G. (2021). From sugar to flowers: A transition of shallow cumulus organization during atomic. *Journal of Advances in Modeling Earth Systems*, *13*(10), e2021MS002619. doi: https://doi.org/10.1029/2021MS002619

Naumann, A. K., Stevens, B., Hohenegger, C., & Mellado, J. P. (2017). A conceptual model of a shallow circulation induced by prescribed low-level radiative cooling. *Journal of the Atmospheric Sciences*, *74*(10), 3129 - 3144. Retrieved from `https://journals.ametsoc.org/view/journals/atsc/74/10/jas-d-17-0030.1.xml` doi: 10.1175/JAS-D-17-0030.1

Nuijens, L., Emanuel, K., Masunaga, H., & L'Ecuyer, T. (2017). Implications of warm rain in shallow cumulus and congestus clouds for large-scale circulations. *Surveys in Geophysics*, *38*(6), 1257–1282. doi: 10.1007/s10712-017-9429-z

Nuijens, L., & Siebesma, A. P. (2019). Boundary Layer Clouds and Convection over Subtropical Oceans in our Current and in a Warmer Climate. *Current Climate*

Change Reports, *5*, 80–94. doi: https://doi.org/10.1007/s40641-019-00126-x

Nuijens, L., & Stevens, B. (2012). The influence of wind speed on shallow marine cumulus convection. *Journal of the Atmospheric Sciences*, *69*(1), 168 - 184. Retrieved from `https://journals.ametsoc.org/view/journals/atsc/69/1/jas-d-11-02.1.xml` doi: 10.1175/JAS-D-11-02.1

Nuijens, L., Stevens, B., & Siebesma, A. P. (2009). The environment of precipitating shallow cumulus convection. *Journal of the Atmospheric Sciences*, *66*(7), 1962-1979. doi: 10.1175/2008JAS2841.1

Pincus, R., Fairall, C. W., Bailey, A., Chen, H., Chuang, P. Y., de Boer, G., ... Zuidema, P. (2021). Observations from the NOAA P-3 aircraft during ATOMIC. *Earth System Science Data Discussions*, *2021*, 1–25. doi: 10.5194/essd-2021-11

Quinn, P. K., Thompson, E., Coffman, D. J., Baidar, S., Bariteau, L., Bates, T. S., ... Zuidema, P. (2021). Measurements from the *RV Ronald H. Brown* and related platforms as part of the Atlantic Tradewind Ocean-Atmosphere Mesoscale Interaction Campaign (ATOMIC). *Earth System Science Data Discussions*, *13*(4), 1–41. doi: 10.5194/essd-2020-331

Rasp, S., Schulz, H., Bony, S., & Stevens, B. (2020). Combining crowd-sourcing and deep learning to explore the meso-scale organization of shallow convection. *Bulletin of the American Meteorological Society*, *101*(11), E1980–E1995. doi: 10.1175/BAMS-D-19-0324.1

Rauber, R. M., Stevens, B., Ochs, H. T., Knight, C., Albrecht, B. A., Blyth, A. M., ... Zuidema, P. (2007). Rain in Shallow Cumulus Over the Ocean: The RICO Campaign. *Bulletin of the American Meteorological Society*, *88*(12), 1912 - 1928. doi: 10.1175/BAMS-88-12-1912

Rieck, M., Nuijens, L., & Stevens, B. (2012). Marine boundary layer cloud feedbacks in a constant relative humidity atmosphere. *Journal of the Atmospheric Sciences*, *69*(8), 2538 - 2550. doi: 10.1175/JAS-D-11-0203.1

Rolph, G., Stein, A., & Stunder, B. (2017). Real-time Environmental Applications and Display sYstem: READY. *Environmental Modelling and Software*, *95*, 210-228. doi: https://doi.org/10.1016/j.envsoft.2017.06.025

Schulz, H. (2021). C^{3}ontext: A common consensus on convective organization during the eurec^{4}a experiment. *Earth System Science Data Discussions*, *2021*, 1–27.

Retrieved from https://essd.copernicus.org/preprints/essd-2021-427/ doi: 10.5194/essd-2021-427

Schulz, H., Eastman, R., & Stevens, B. (2021). Characterization and evolution of organized shallow convection in the downstream north atlantic trades. *Journal of Geophysical Research: Atmospheres*, *126*(17), e2021JD034575. doi: https://doi.org/10.1029/2021JD034575

Seifert, A., & Heus, T. (2013). Large-eddy simulation of organized precipitating trade wind cumulus clouds. *Atmospheric Chemistry and Physics*, *13*(11), 5631–5645. doi: 10.5194/acp-13-5631-2013

Stein, A. F., Draxler, R. R., Rolph, G. D., Stunder, B. J. B., Cohen, M. D., & Ngan, F. (2015). NOAA's HYSPLIT Atmospheric Transport and Dispersion Modeling System. *Bulletin of the American Meteorological Society*, *96*(12), 2059 - 2077. doi: 10.1175/BAMS-D-14-00110.1

Stephan, C. C., Schnitt, S., Schulz, H., Bellenger, H., de Szoeke, S. P., Acquistapace, C., ... Stevens, B. (2021). Ship- and island-based atmospheric soundings from the 2020 eurec^{4}a field campaign. *Earth System Science Data*, *13*(2), 491–514. doi: 10.5194/essd-13-491-2021

Stevens, B., Ackerman, A. S., Albrecht, B. A., Brown, A. R., Chlond, A., Cuxart, J., ... Stevens, D. E. (2001). Simulations of trade wind cumuli under a strong inversion. *Journal of the Atmospheric Sciences*, *58*(14), 1870 - 1891. doi: 10.1175/1520-0469(2001)058⟨1870:SOTWCU⟩2.0.CO;2

Stevens, B., Bony, S., Brogniez, H., Hentgen, L., Hohenegger, C., Kiemle, C., ... Zuidema, P. (2020). Sugar, gravel, fish and flowers: Mesoscale cloud patterns in the trade winds. *Quarterly Journal of the Royal Meteorological Society*, *146*(726), 141–152. doi: 10.1002/qj.3662

Stevens, B., Bony, S., Farrell, D., Ament, F., Blyth, A., Fairall, C., ... Zöger, M. (2021). EUREC^{4}A. *Earth System Science Data Discussions*, *2021*, 1–78. doi: 10.5194/essd-2021-18

vanZanten, M. C., Stevens, B., Nuijens, L., Siebesma, A. P., Ackerman, A. S., Burnet, F., ... Wyszogrodzki, A. (2011). Controls on precipitation and cloudiness in simulations of trade-wind cumulus as observed during RICO. *Journal of Advances in Modeling Earth Systems*, *3*(2). doi: https://doi.org/10.1029/2011MS000056

Vial, J., Vogel, R., Bony, S., Stevens, B., Winker, D. M., Cai, X., ... Brogniez, H. (2019). A new look at the daily cycle of trade wind cumuli. *Journal of Advances in Modeling Earth Systems*, *11*(10), 3148-3166. doi: https://doi.org/10.1029/2019MS001746

Vial, J., Vogel, R., & Schulz, H. (2021). On the daily cycle of mesoscale cloud organization in the winter trades. *Quarterly Journal of the Royal Meteorological Society*, *147*(738), 2850-2873. doi: 10.1002/qj.4103

Vogel, R., Konow, H., Schulz, H., & Zuidema, P. (2021). A climatology of trade-wind cumulus cold pools and their link to mesoscale cloud organization. *Atmospheric Chemistry and Physics*, *21*(21), 16609–16630. Retrieved from `https://acp.copernicus.org/articles/21/16609/2021/` doi: 10.5194/acp-21-16609-2021

Xu, K.-M., Cheng, A., & Zhang, M. (2010). Cloud-resolving simulation of low-cloud feedback to an increase in sea surface temperature. *Journal of the Atmospheric Sciences*, *67*(3), 730 - 748. doi: 10.1175/2009JAS3239.1

Zelinka, M. D., Myers, T. A., McCoy, D. T., Po-Chedley, S., Caldwell, P. M., Ceppi, P., ... Taylor, K. E. (2020). Causes of higher climate sensitivity in CMIP6 models. *Geophysical Research Letters*, *47*(1), e2019GL085782. doi: https://doi.org/10.1029/2019GL085782

Zelinka, M. D., Zhou, C., & Klein, S. A. (2016). Insights from a refined decomposition of cloud feedbacks. *Geophysical Research Letters*, *43*, 9259–9269. doi: 10.1002/2016GL069917

Zhang, M., Bretherton, C. S., Blossey, P. N., Austin, P. H., Bacmeister, J. T., Bony, S., ... Zhao, M. (2013). CGILS: Results from the first phase of an international project to understand the physical mechanisms of low cloud feedbacks in single column models. *Journal of Advances in Modeling Earth Systems*, *5*(4), 826–842. doi: 10.1002/2013MS000246

Zuidema, P., Li, Z., Hill, R. J., Bariteau, L., Rilling, B., Fairall, C., ... Hare, J. (2012). On trade wind cumulus cold pools. *Journal of the Atmospheric Sciences*, *69*(1), 258 - 280. doi: 10.1175/JAS-D-11-0143.1

Zuidema, P., Sedlacek III, A. J., Flynn, C., Springston, S., Delgadillo, R., Zhang, J., ... Muradyan, P. (2018). The Ascension Island boundary layer in the remote Southeast Atlantic is often smoky. *Geophysical Research Letters*, *45*(9),

4456-4465. doi: https://doi.org/10.1002/2017GL076926

Zuidema, P., Torri, G., Muller, C., & Chandra, A. (2017). A survey of precipitation-induced atmospheric cold pools over oceans and their interactions with the larger-scale environment. *Surveys in Geophysics*, *38*(6), 1283–1305. doi: 10.1007/s10712-017-9447-x

Figure 1.

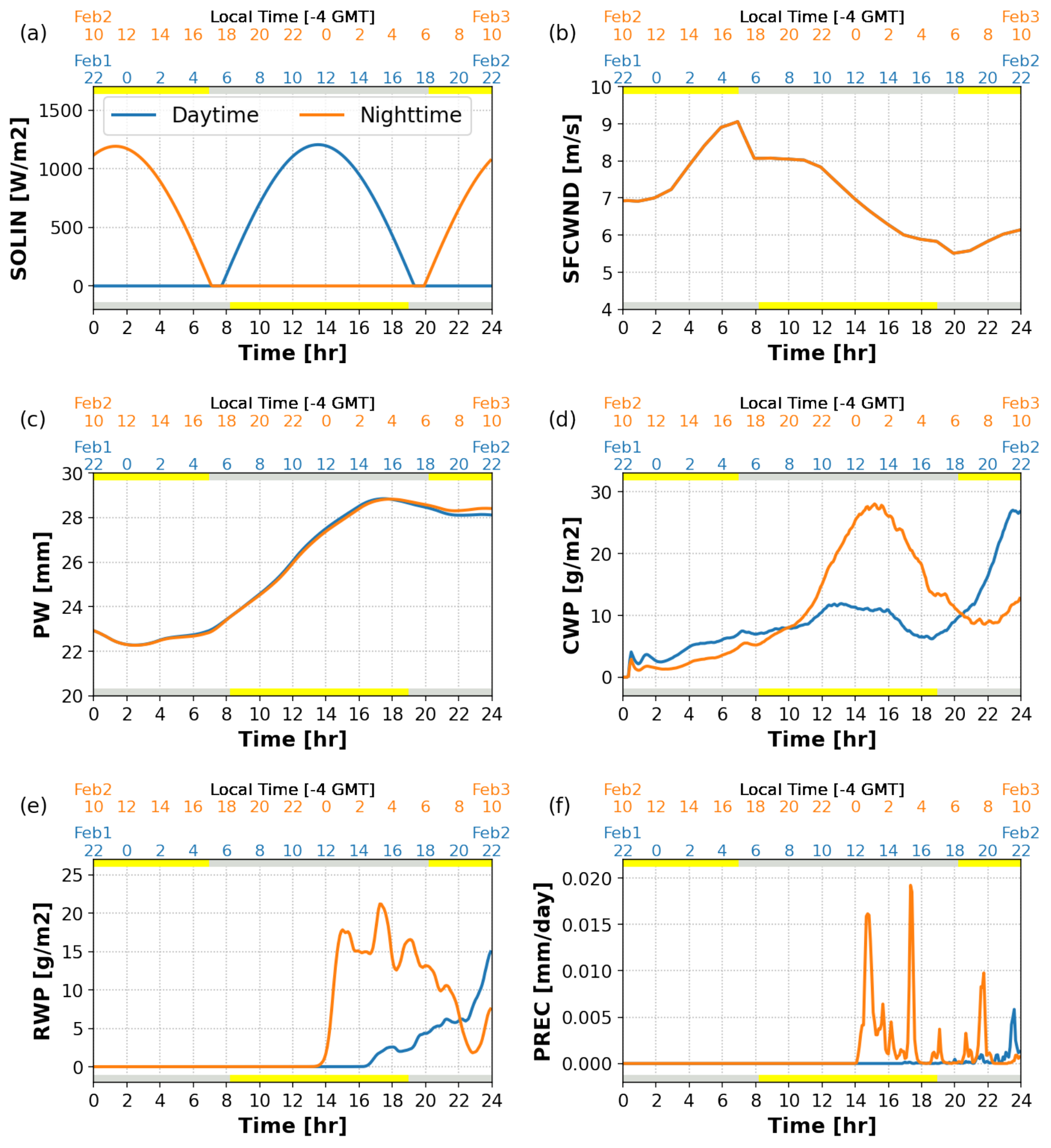
(a)
Local Time [-4 GMT]
Feb2
Feb3
Feb1
Daytime
Nighttime
SOLIN [W/m2]
Time [hr]
(b)
SFCWND [m/s]
Time [hr]
(c)
PW [mm]
Time [hr]
(d)
CWP [g/m2]
Time [hr]
(e)
RWP [g/m2]
Time [hr]
(f)
PREC [mm/day]
Time [hr]

Figure 2.

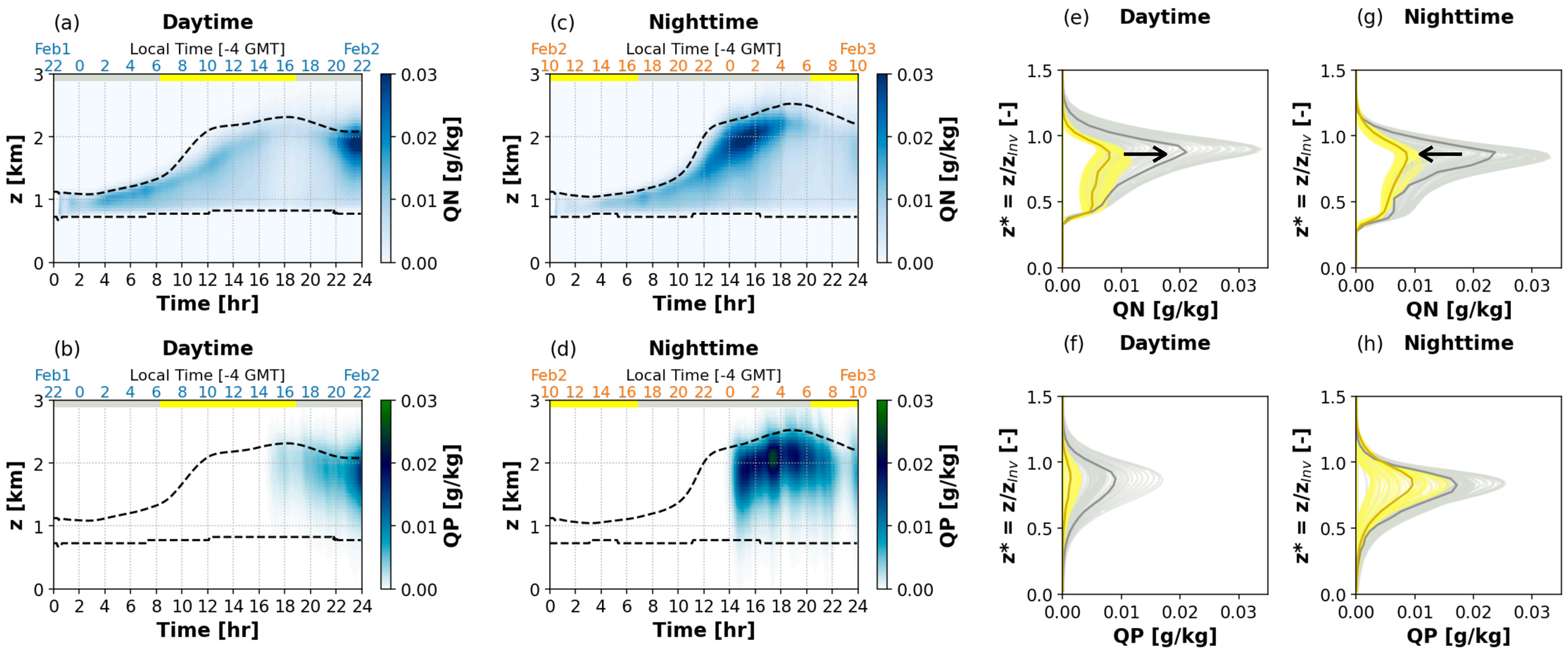
(a) Daytime
Feb1
Local Time [-4 GMT]
Feb2
22 0 2 4 6 8 10 12 14 16 18 20 22
z [km]
Time [hr]
QN [g/kg]
(b) Daytime
QP [g/kg]
(c) Nighttime
Feb2
Feb3
10 12 14 16 18 20 22 0 2 4 6 8 10
(d) Nighttime
(e) Daytime
(f) Daytime
(g) Nighttime
(h) Nighttime
z* = z/z_inv [-]

Figure 3.

14 hr (12:00)
16 hr (14:00)
18 hr (16:00)
20 hr (18:00)
22 hr (20:00)
24 hr (22:00)
y [km]
x [km]
0
48
96
144
192
Daytime CLD [%]
0
20
40
60
80
100
Daytime TWP [mm]
24
26
28
30
32
34

Figure 4.

14 hr (00:00)
16 hr (02:00)
18 hr (04:00)
20 hr (06:00)
22 hr (08:00)
24 hr (10:00)
y [km]
x [km]
0
48
96
144
192
Nighttime CLD [%]
0
20
40
60
80
100
Nighttime TWP [mm]
24
26
28
30
32
34

Figure 5.

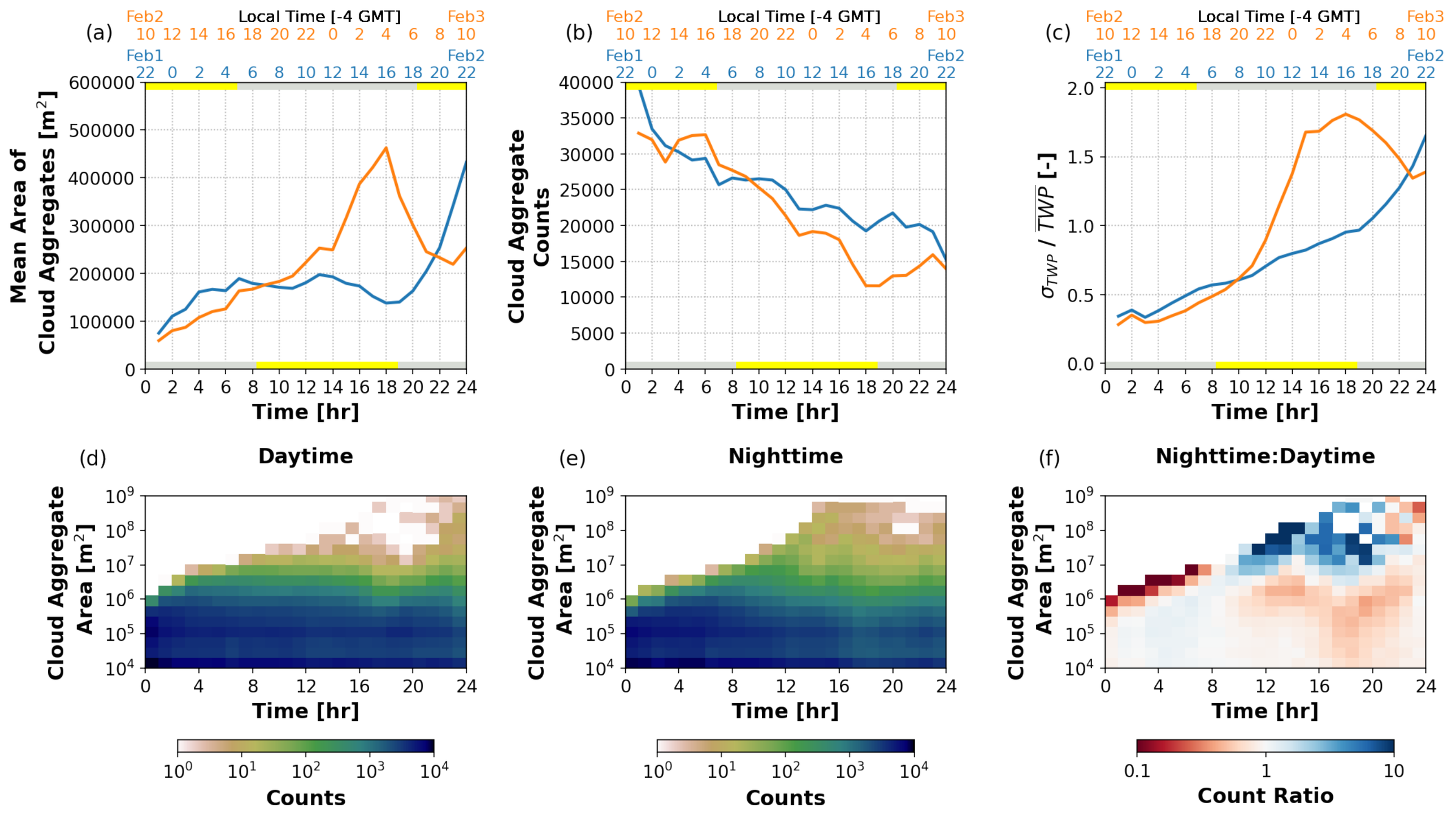
(a)
Local Time [-4 GMT]
Feb2
Feb3
Feb1
Mean Area of Cloud Aggregates [m^2]
Time [hr]
(b)
Cloud Aggregate Counts
Time [hr]
(c)
σ_{TWP} / $\overline{TWP}$ [-]
Time [hr]
(d)
Daytime
Cloud Aggregate Area [m^2]
Time [hr]
Counts
(e)
Nighttime
Cloud Aggregate Area [m^2]
Time [hr]
Counts
(f)
Nighttime:Daytime
Cloud Aggregate Area [m^2]
Time [hr]
Count Ratio

Figure 6.

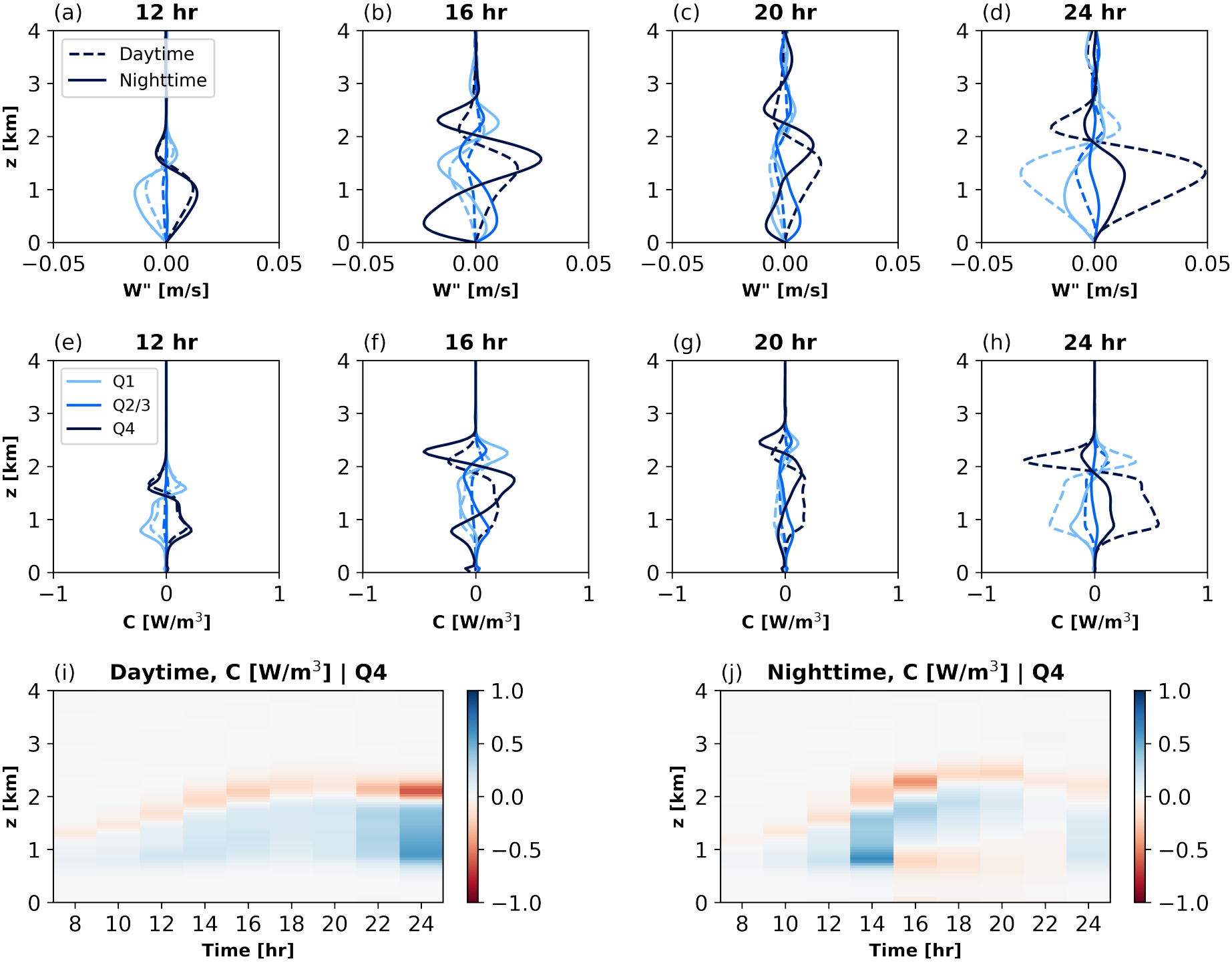
(a) 12 hr
(b) 16 hr
(c) 20 hr
(d) 24 hr
Daytime
Nighttime
z [km]
W" [m/s]
(e) 12 hr
(f) 16 hr
(g) 20 hr
(h) 24 hr
Q1
Q2/3
Q4
C [W/m3]
(i) Daytime, C [W/m3] | Q4
(j) Nighttime, C [W/m3] | Q4
Time [hr]

Figure 7.

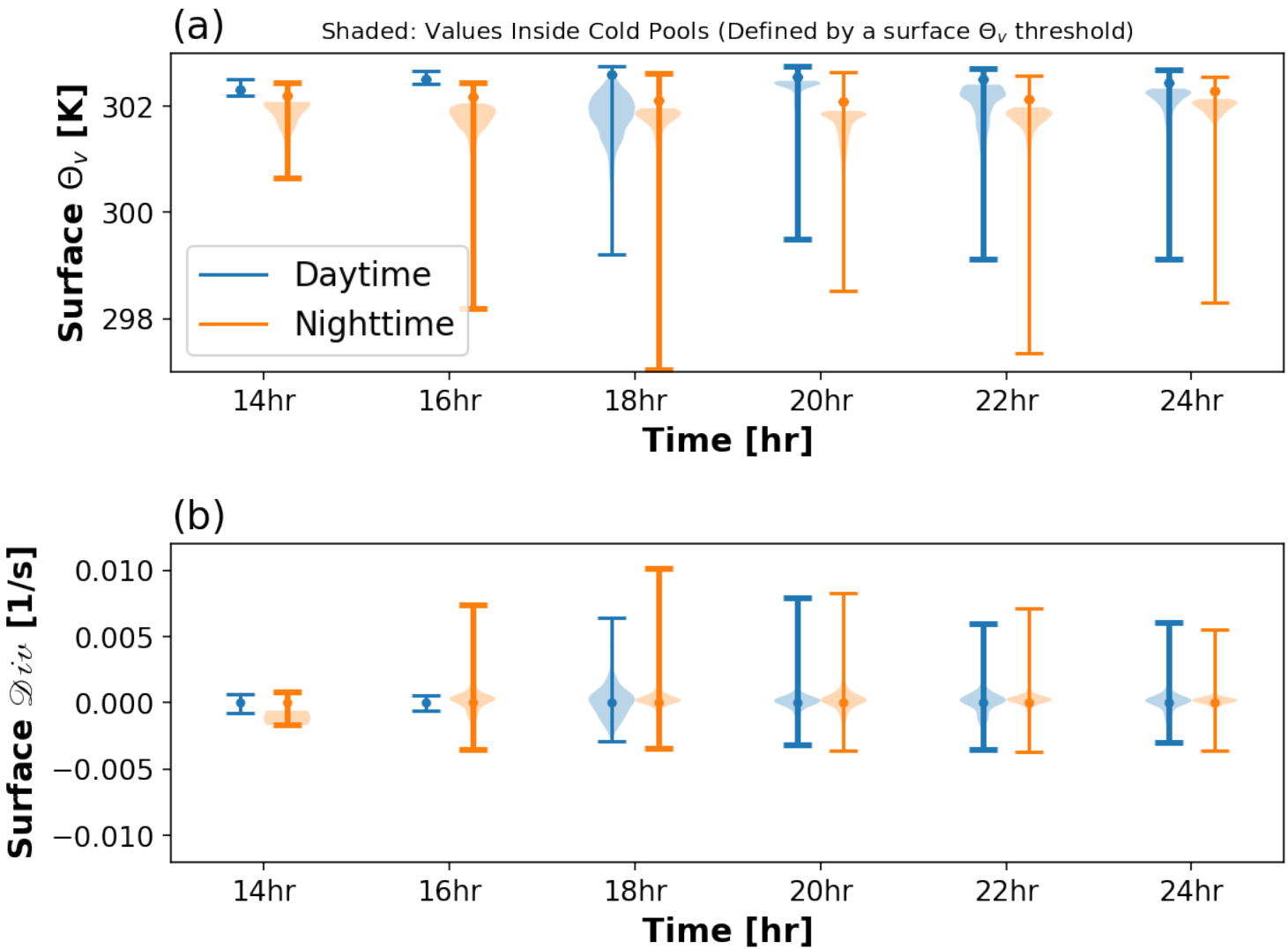
(a)
Shaded: Values Inside Cold Pools (Defined by a surface Θ_v threshold)
Surface Θ_v [K]
302
300
298
Daytime
Nighttime
14hr
16hr
18hr
20hr
22hr
24hr
Time [hr]
(b)
Surface $\mathscr{D}iv$ [1/s]
0.010
0.005
0.000
−0.005
−0.010
14hr
16hr
18hr
20hr
22hr
24hr
Time [hr]

Figure 8.

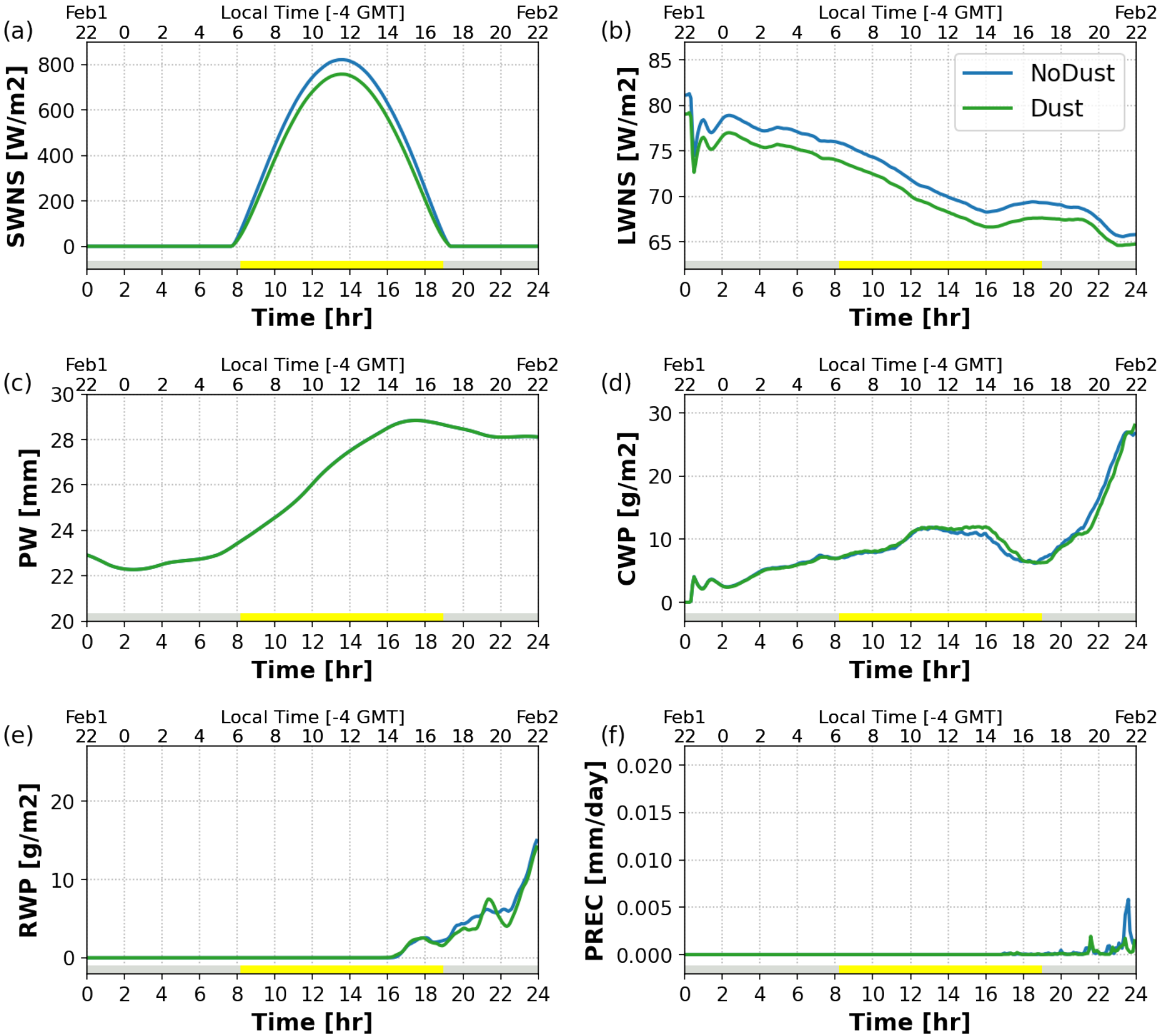
(a)
Feb1
Local Time [-4 GMT]
Feb2
22 0 2 4 6 8 10 12 14 16 18 20 22
SWNS [W/m2]
800
600
400
200
0
0 2 4 6 8 10 12 14 16 18 20 22 24
Time [hr]
(b)
Feb1
Local Time [-4 GMT]
Feb2
22 0 2 4 6 8 10 12 14 16 18 20 22
LWNS [W/m2]
85
80
75
70
65
NoDust
Dust
0 2 4 6 8 10 12 14 16 18 20 22 24
Time [hr]
(c)
Feb1
Local Time [-4 GMT]
Feb2
22 0 2 4 6 8 10 12 14 16 18 20 22
PW [mm]
30
28
26
24
22
20
0 2 4 6 8 10 12 14 16 18 20 22 24
Time [hr]
(d)
Feb1
Local Time [-4 GMT]
Feb2
22 0 2 4 6 8 10 12 14 16 18 20 22
CWP [g/m2]
30
20
10
0
0 2 4 6 8 10 12 14 16 18 20 22 24
Time [hr]
(e)
Feb1
Local Time [-4 GMT]
Feb2
22 0 2 4 6 8 10 12 14 16 18 20 22
RWP [g/m2]
20
10
0
0 2 4 6 8 10 12 14 16 18 20 22 24
Time [hr]
(f)
Feb1
Local Time [-4 GMT]
Feb2
22 0 2 4 6 8 10 12 14 16 18 20 22
PREC [mm/day]
0.020
0.015
0.010
0.005
0.000
0 2 4 6 8 10 12 14 16 18 20 22 24
Time [hr]

Figure 9.

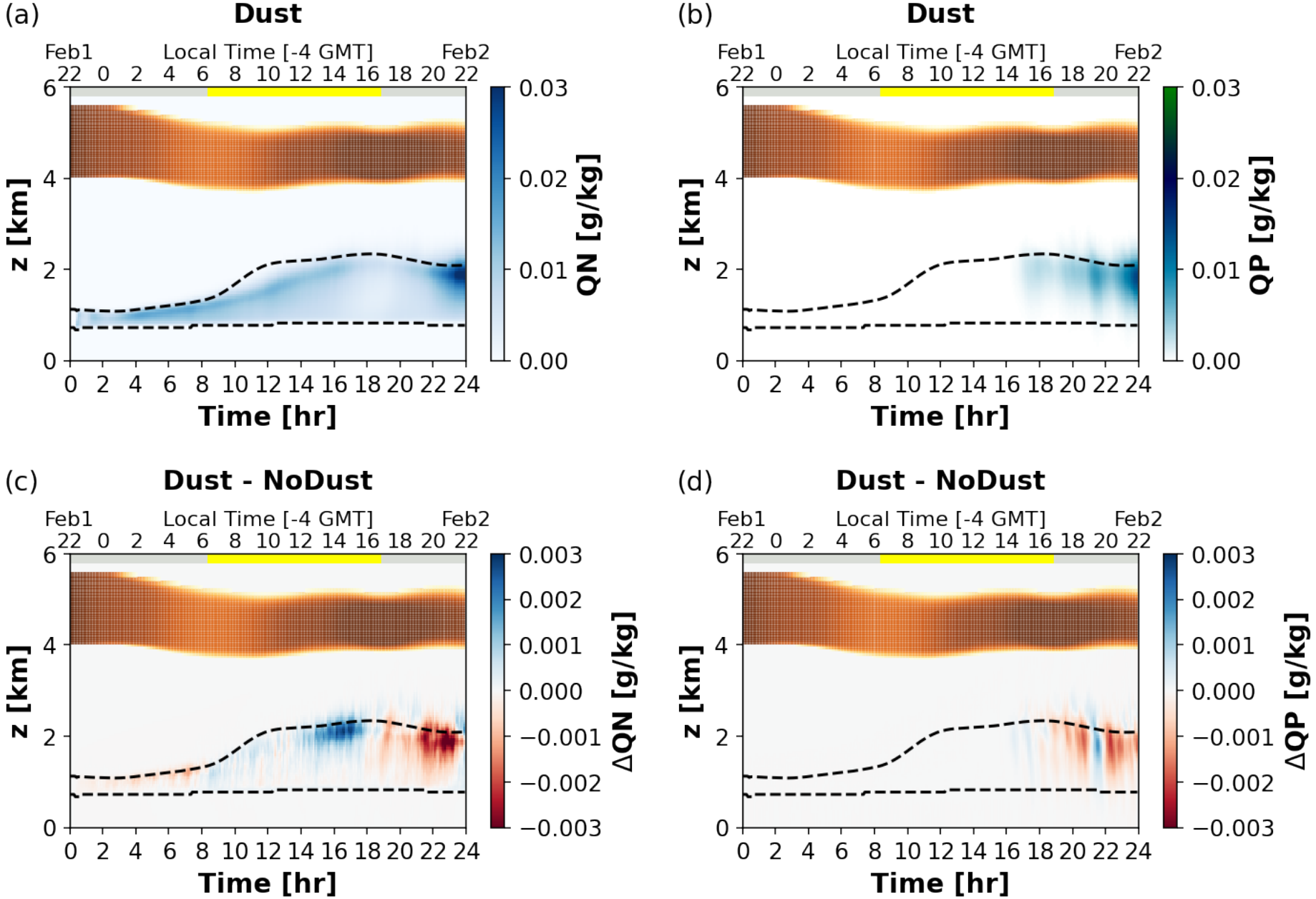
(a)
Dust
Feb1
Local Time [-4 GMT]
Feb2
22 0 2 4 6 8 10 12 14 16 18 20 22
z [km]
Time [hr]
QN [g/kg]
0.03
0.02
0.01
0.00
(b)
Dust
QP [g/kg]
(c)
Dust - NoDust
ΔQN [g/kg]
0.003
0.002
0.001
0.000
−0.001
−0.002
−0.003
(d)
Dust - NoDust
ΔQP [g/kg]

Figure 10.

14 hr (12:00)
16 hr (14:00)
18 hr (16:00)
20 hr (18:00)
22 hr (20:00)
24 hr (22:00)
y [km]
x [km]
0
48
96
144
192
Dust CLD [%]
0
20
40
60
80
100
Dust TWP [mm]
24
26
28
30
32
34

Figure 11.

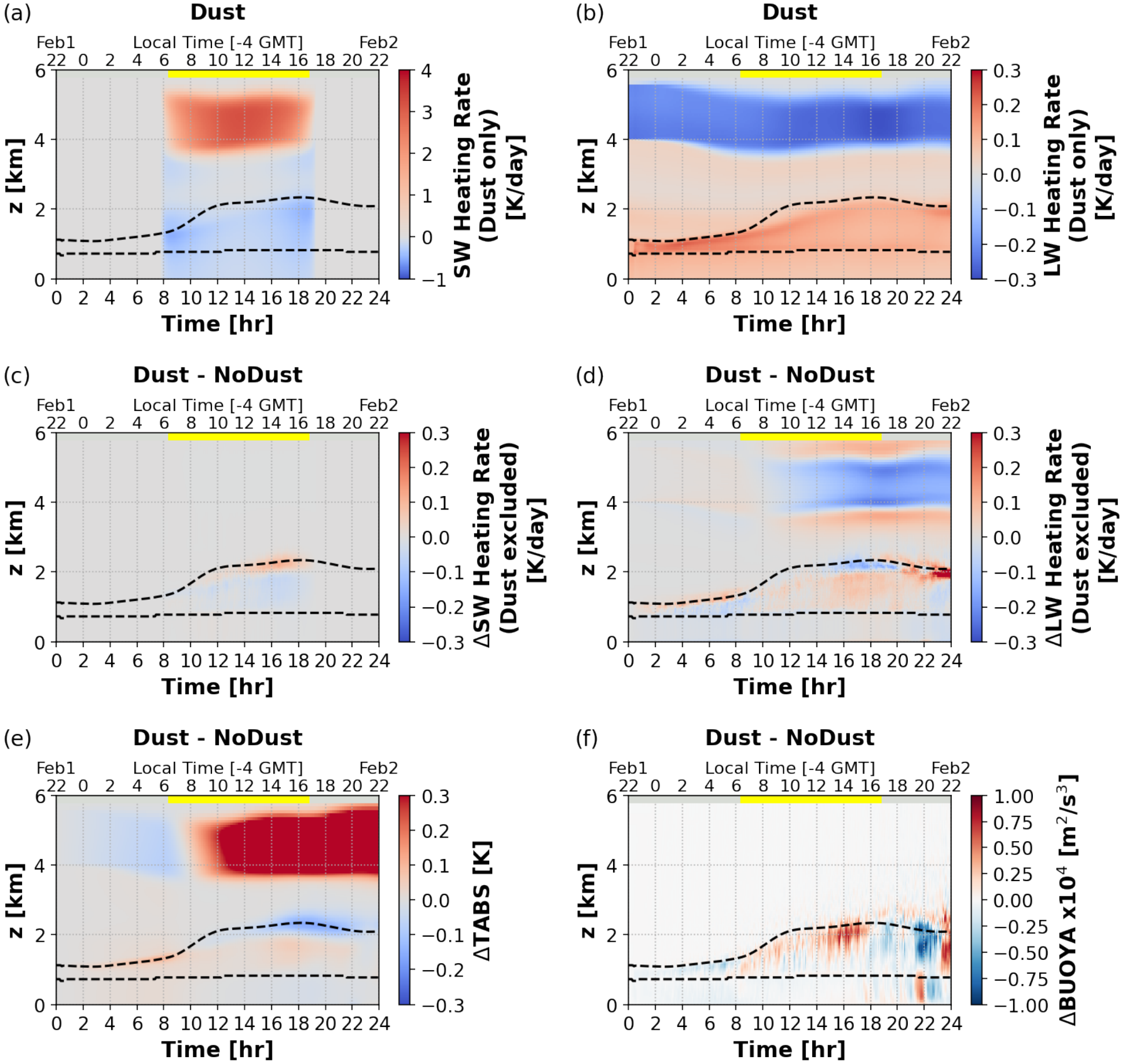
(a)
Dust
Feb1
Local Time [-4 GMT]
Feb2
22 0 2 4 6 8 10 12 14 16 18 20 22
z [km]
Time [hr]
SW Heating Rate (Dust only) [K/day]
(b)
Dust
LW Heating Rate (Dust only) [K/day]
(c)
Dust - NoDust
ΔSW Heating Rate (Dust excluded) [K/day]
(d)
Dust - NoDust
ΔLW Heating Rate (Dust excluded) [K/day]
(e)
Dust - NoDust
ΔTABS [K]
(f)
Dust - NoDust
ΔBUOYA x10⁴ [m²/s³]

Figure 12.

Feb 2, 18 hr (16:00)

(a) CLD [%]

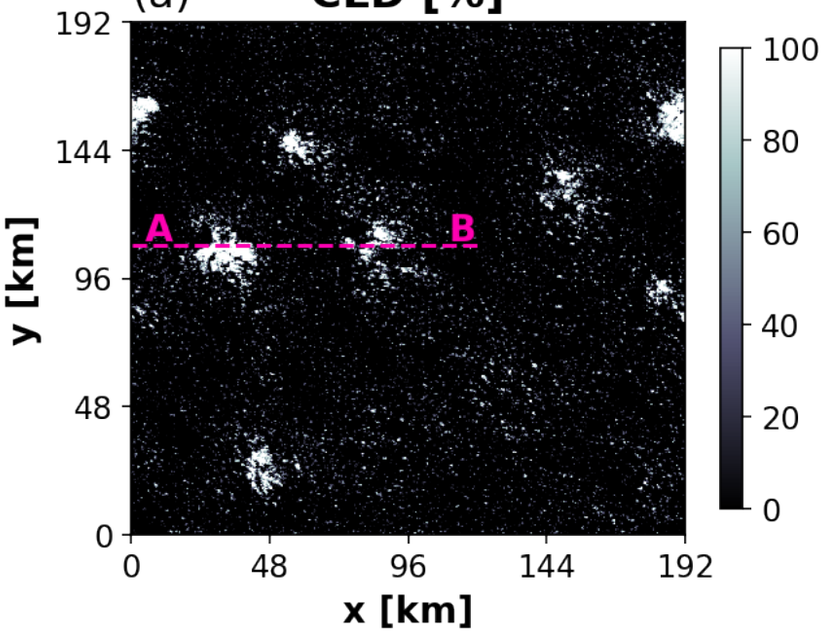

(b) MD [#/mg]

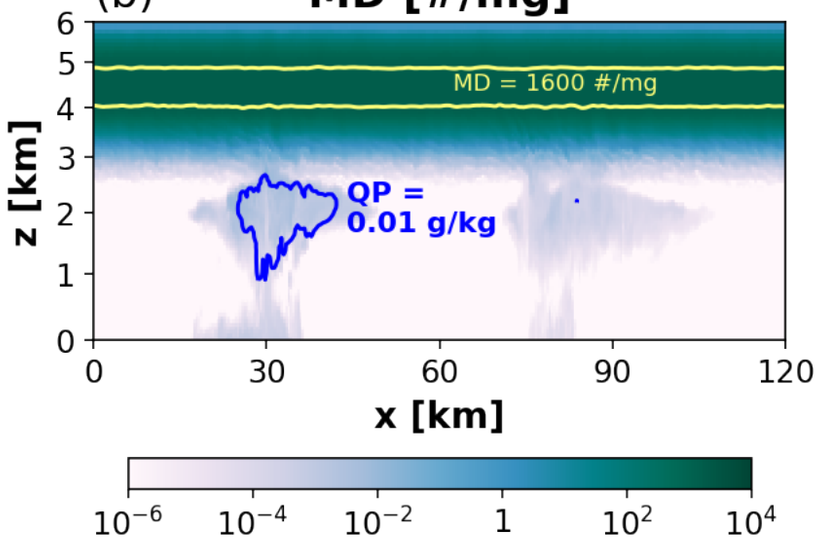

(c) QN [g/kg]

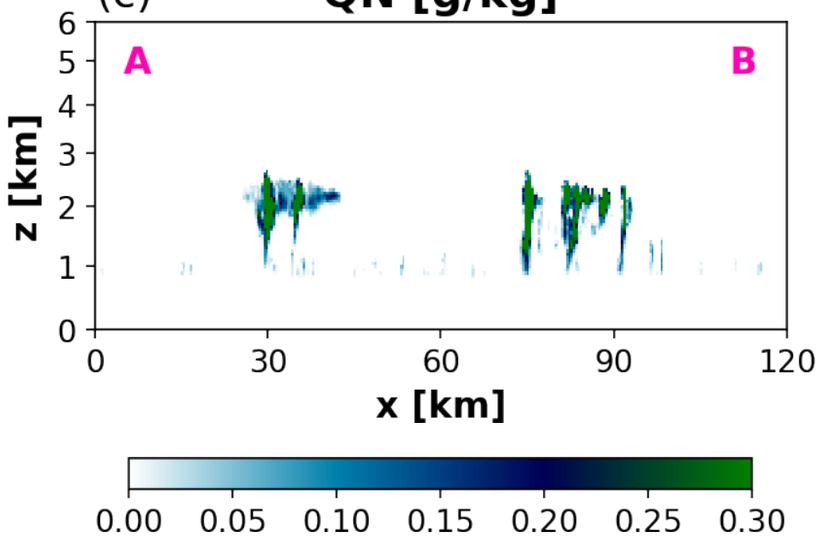

(d) SW | Dust only [K/day]

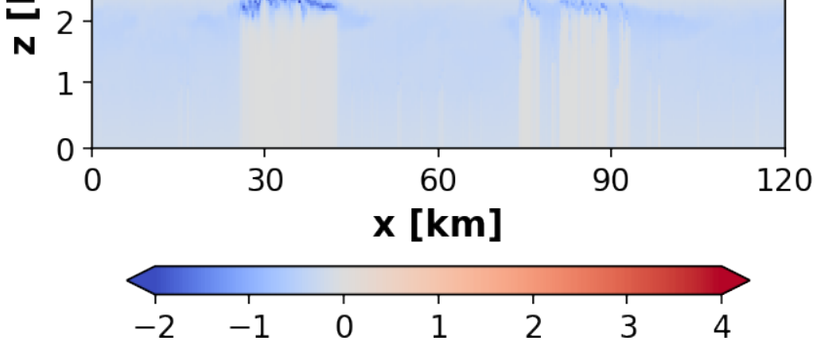

(e) LW | Dust only [K/day]

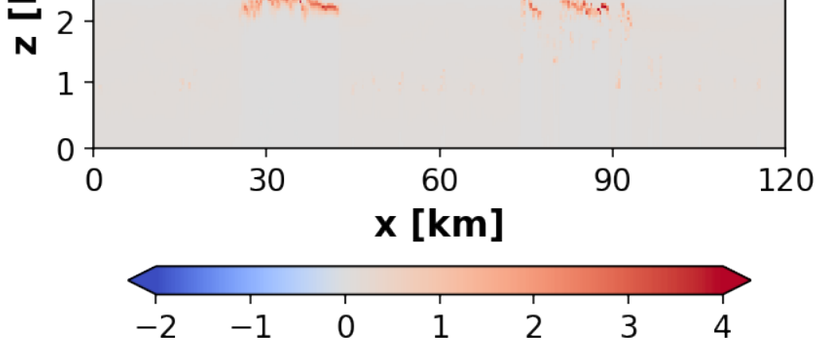

(f) RAD | Dust only [K/day]

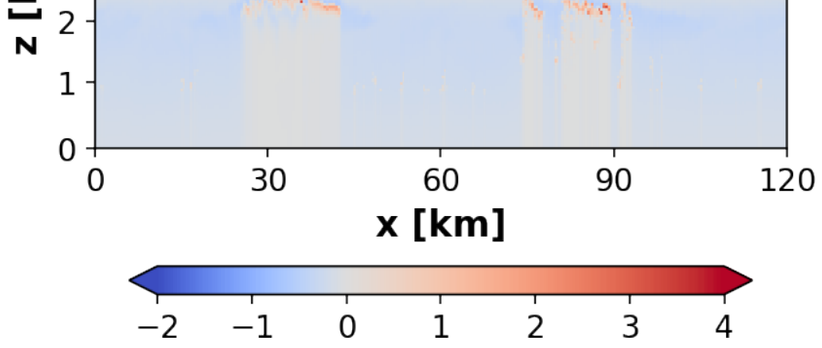

(g) SW | The rest [K/day]

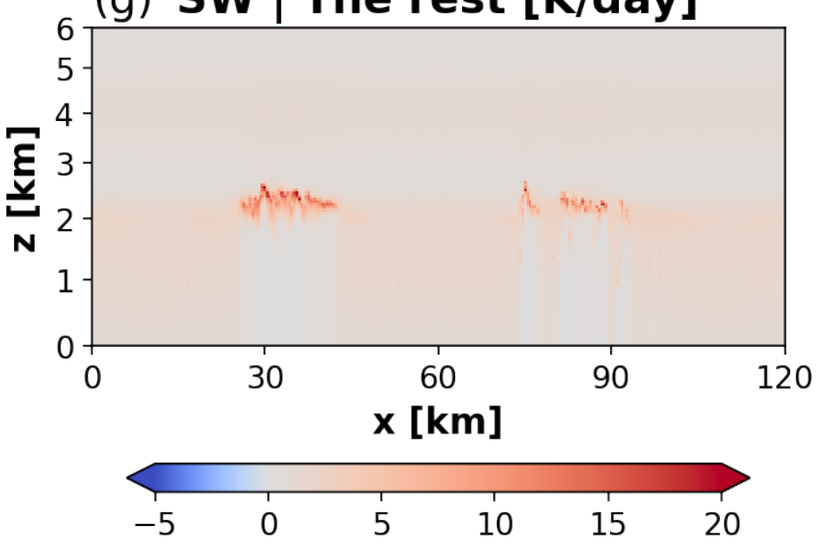

(h) LW | The rest [K/day]

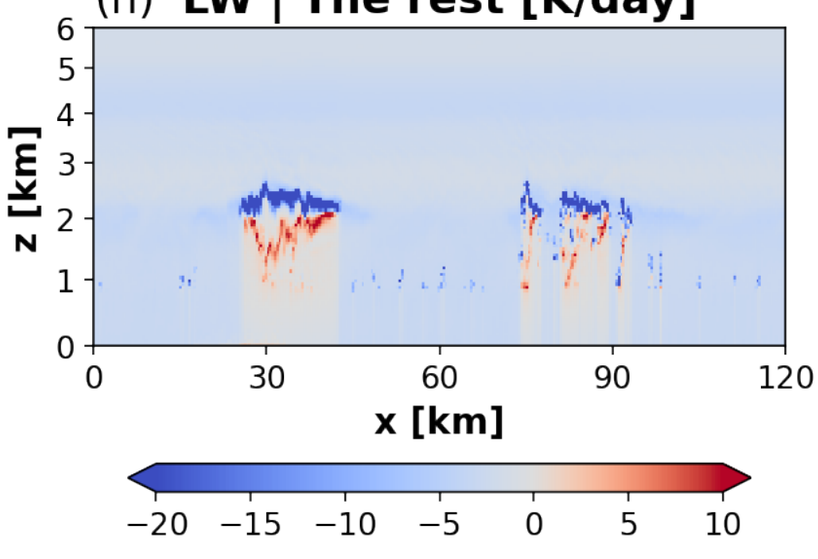

(i) TABS [K]

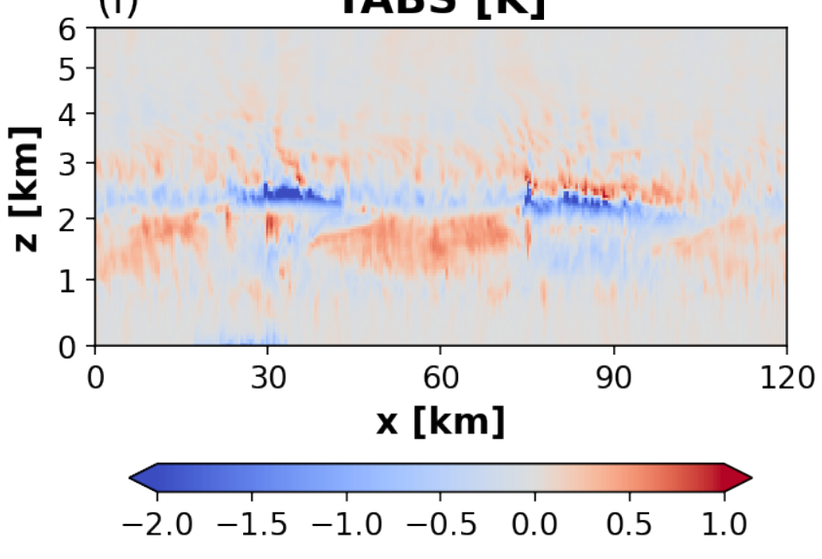

Figure 14.

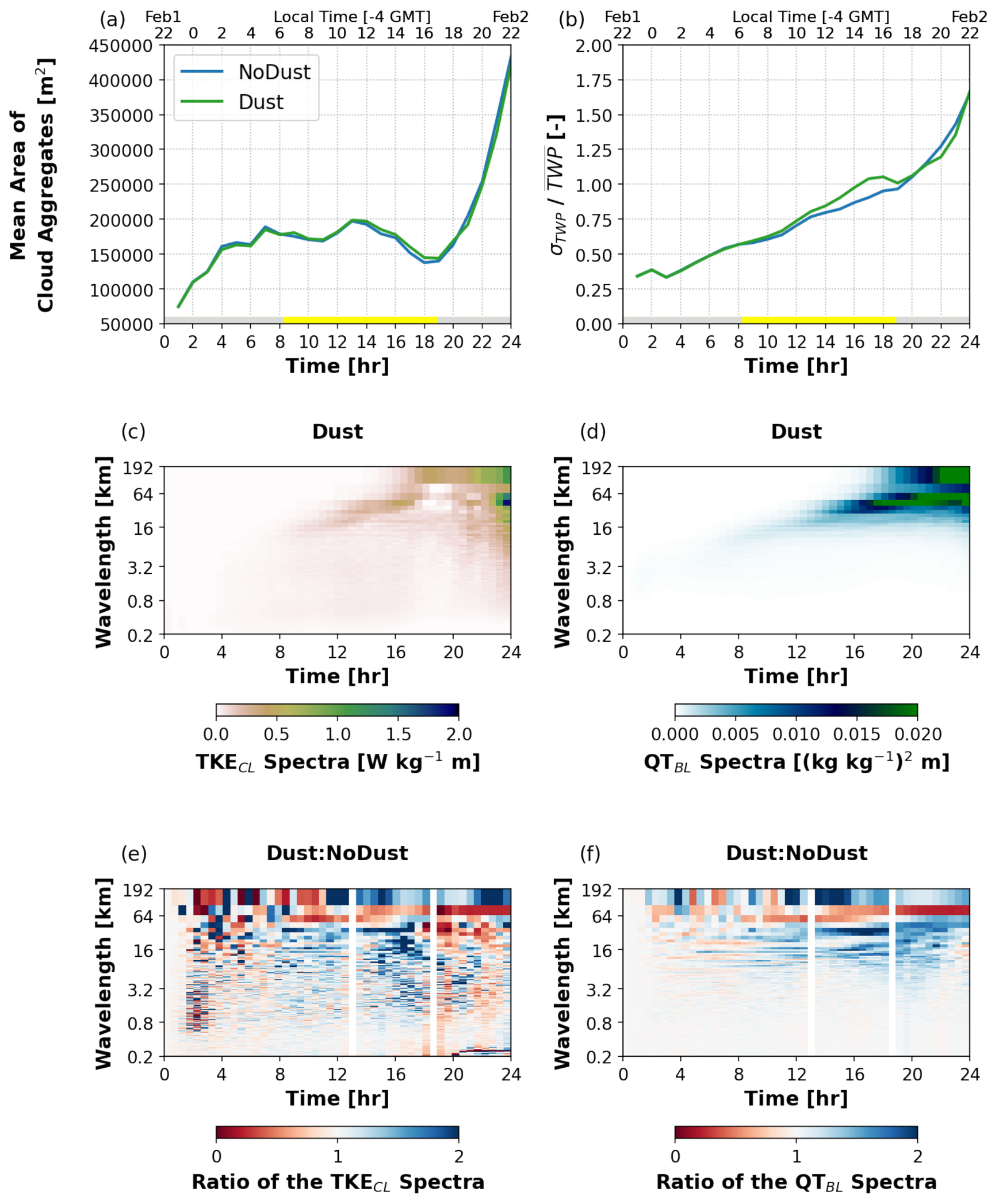
(a)
Feb1
Local Time [-4 GMT]
Feb2
22 0 2 4 6 8 10 12 14 16 18 20 22
NoDust
Dust
Mean Area of Cloud Aggregates [m^2]
Time [hr]
(b)
σ_{TWP} / $\overline{TWP}$ [-]
(c)
Dust
Wavelength [km]
192
64
16
3.2
0.8
0.2
TKE$_{CL}$ Spectra [W kg^{-1} m]
(d)
QT$_{BL}$ Spectra [(kg kg^{-1})^2 m]
(e)
Dust:NoDust
Ratio of the TKE$_{CL}$ Spectra
(f)
Ratio of the QT$_{BL}$ Spectra

Figure 13.

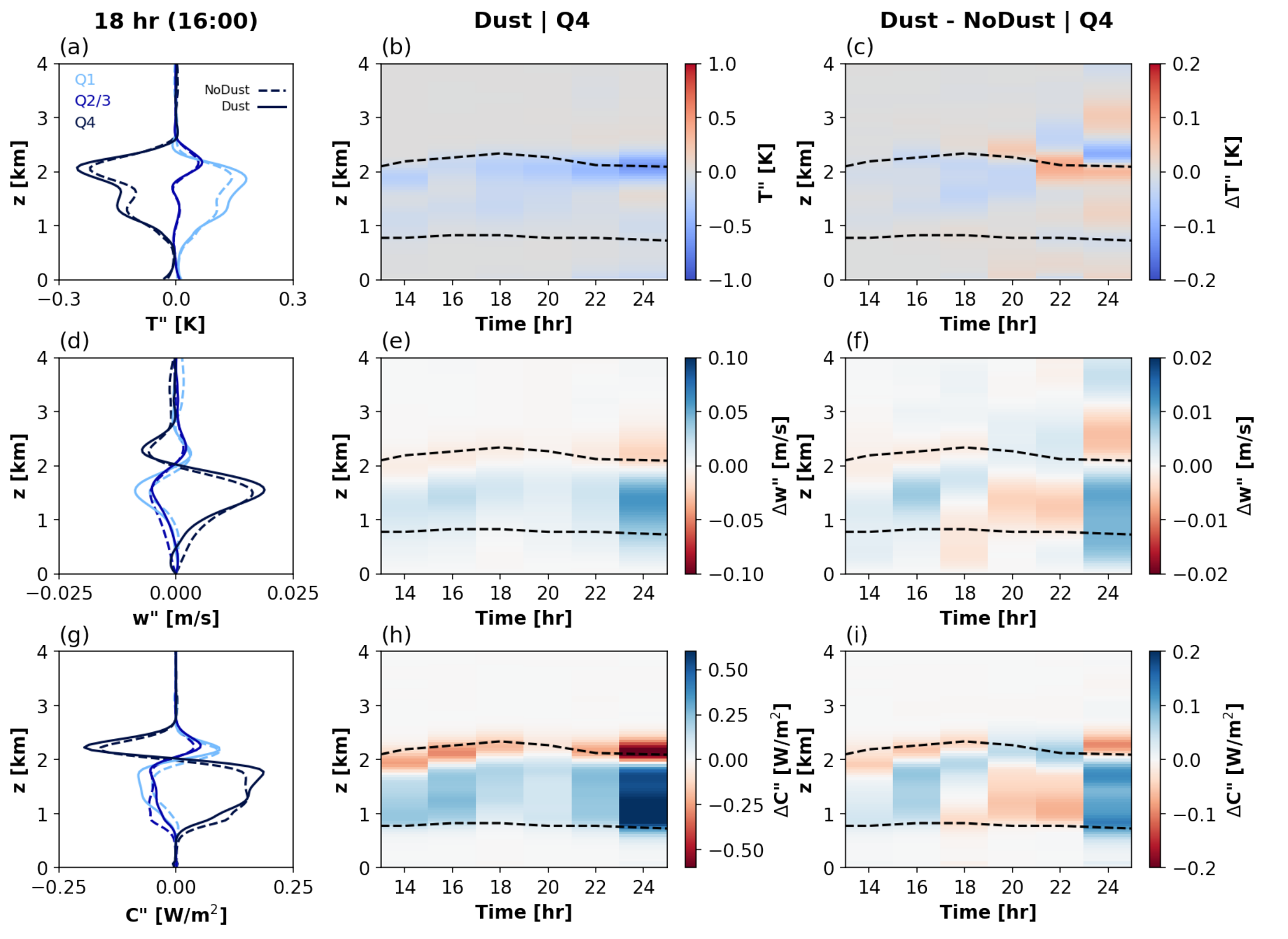
18 hr (16:00)
Dust | Q4
Dust - NoDust | Q4
(a)
(b)
(c)
(d)
(e)
(f)
(g)
(h)
(i)
Q1
Q2/3
Q4
NoDust
Dust
z [km]
T" [K]
Time [hr]
ΔT" [K]
w" [m/s]
Δw" [m/s]
C" [W/m^2]
ΔC" [W/m^2]

Figure 15.

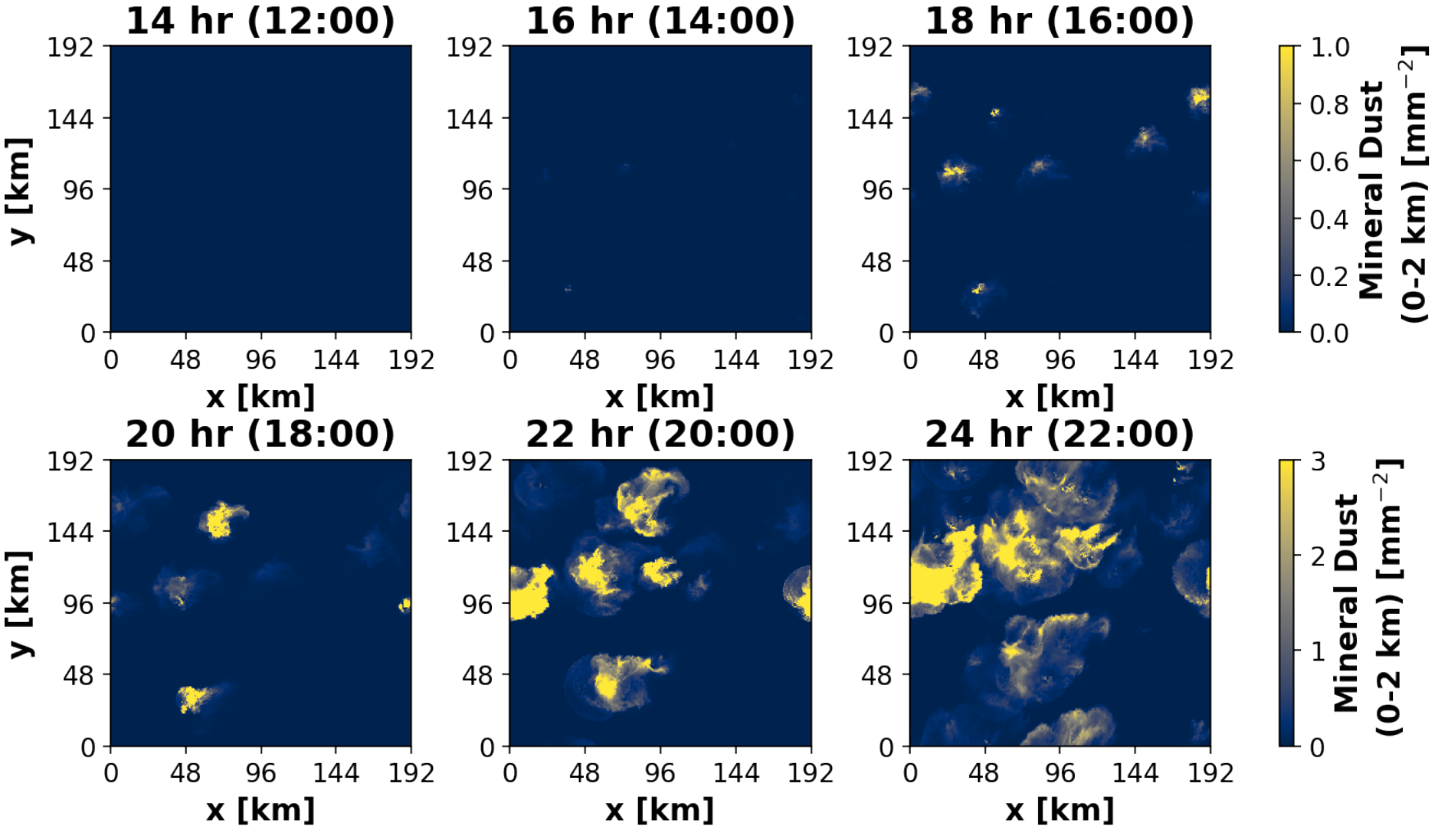
14 hr (12:00)
16 hr (14:00)
18 hr (16:00)
20 hr (18:00)
22 hr (20:00)
24 hr (22:00)
y [km]
x [km]
0
48
96
144
192
Mineral Dust
(0-2 km) [mm^{-2}]
0.0
0.2
0.4
0.6
0.8
1.0
0
1
2
3

Figure B1.

Daytime

8hr | 10hr | 12hr | 14hr | 16 hr | 18hr | 20hr | 22hr | 24hr

z [km]

A [W/m^3]

F [W/m^3]

C [W/m^3]

S [W/m^3]

Figure B2.

Nighttime

8hr | 10hr | 12hr | 14hr | 16 hr | 18hr | 20hr | 22hr | 24hr

z [km]

A [W/m^3]

F [W/m^3]

C [W/m^3]

S [W/m^3]

Figure B4.

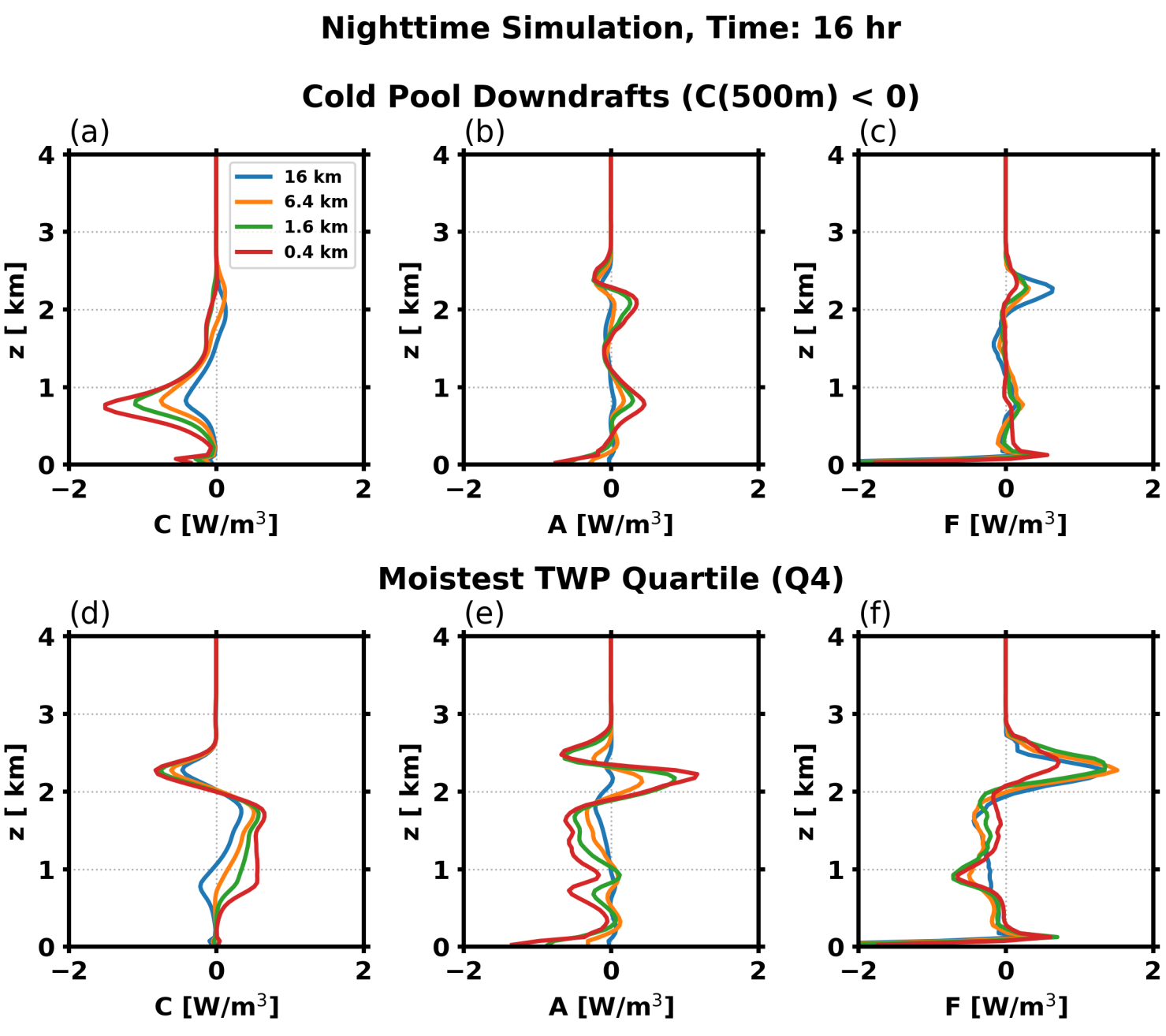
Nighttime Simulation, Time: 16 hr
Cold Pool Downdrafts (C(500m) < 0)
(a)
(b)
(c)
16 km
6.4 km
1.6 km
0.4 km
z [km]
C [W/m3]
A [W/m3]
F [W/m3]
Moistest TWP Quartile (Q4)
(d)
(e)
(f)

Figure B5.

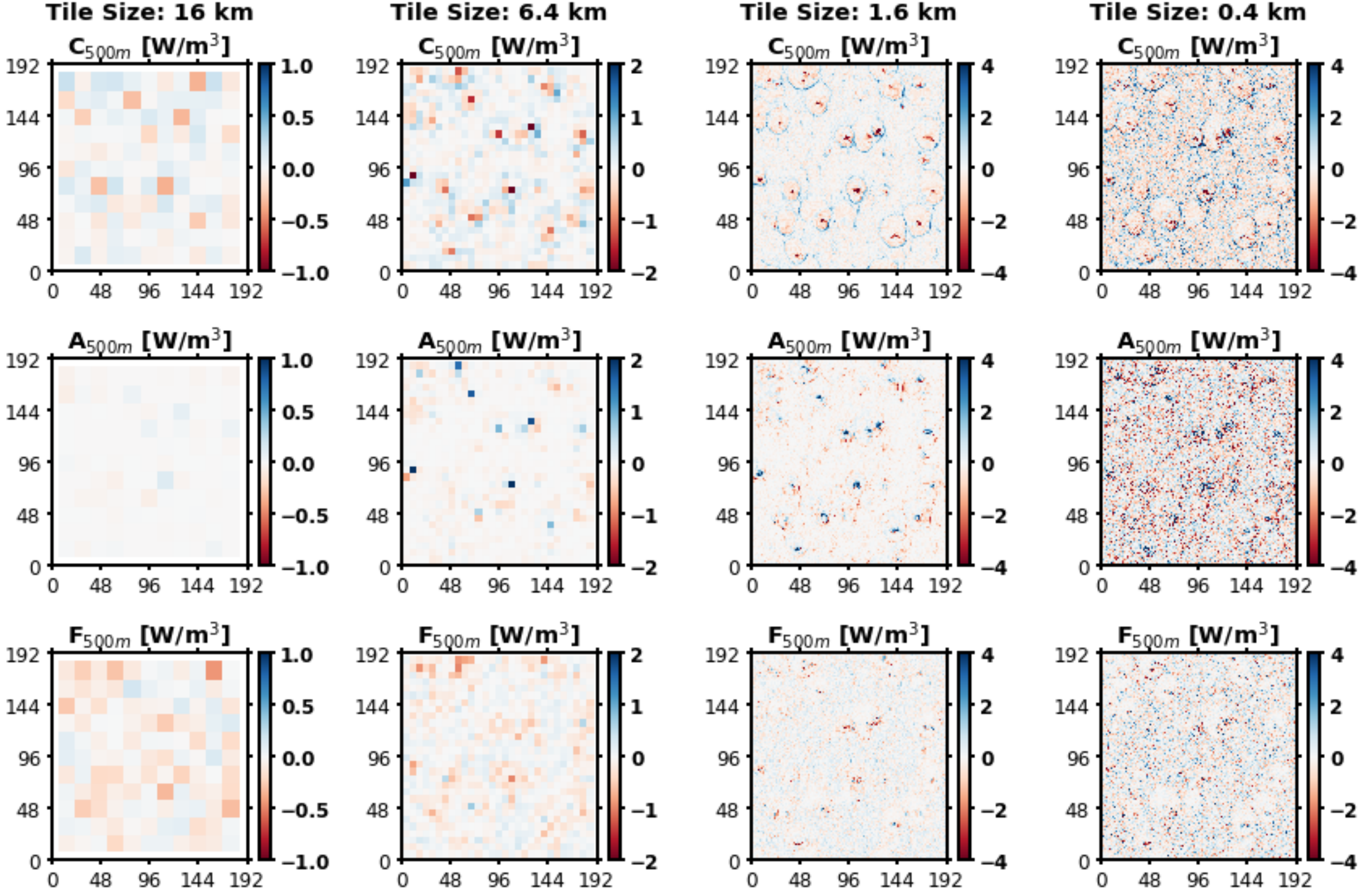
Tile Size: 16 km
Tile Size: 6.4 km
Tile Size: 1.6 km
Tile Size: 0.4 km
C_{500m} [W/m^3]
A_{500m} [W/m^3]
F_{500m} [W/m^3]
0
48
96
144
192
1.0
0.5
0.0
−0.5
−1.0
2
1
0
−1
−2
4
2
0
−2
−4

Figure B3.

Dust

8hr | 10hr | 12hr | 14hr | 16 hr | 18hr | 20hr | 22hr | 24hr

z [km]

A [W/m^3]

F [W/m^3]

C [W/m^3]

S [W/m^3]

Figure A1.

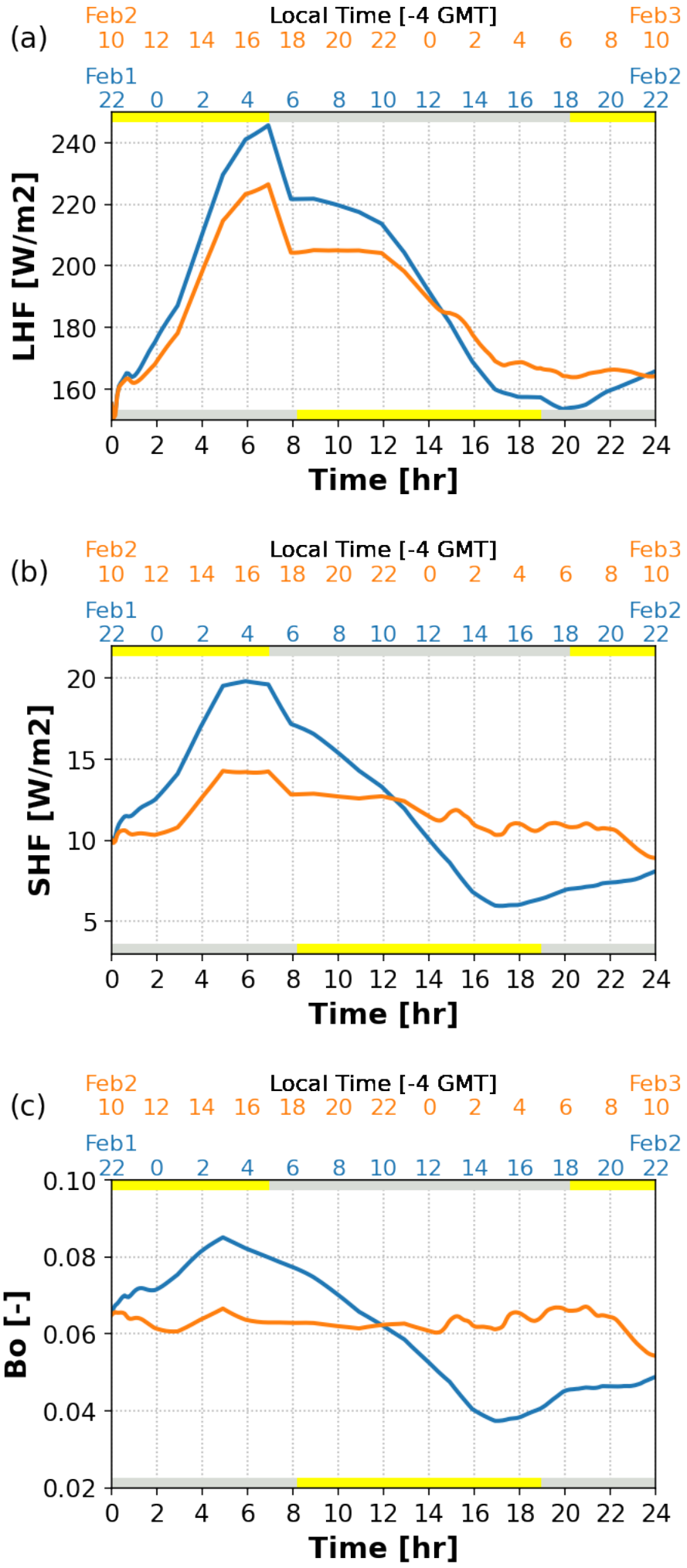
(a)
Local Time [-4 GMT]
Feb2
Feb3
Feb1
Feb2
LHF [W/m2]
Time [hr]
(b)
Local Time [-4 GMT]
Feb2
Feb3
Feb1
Feb2
SHF [W/m2]
Time [hr]
(c)
Local Time [-4 GMT]
Feb2
Feb3
Feb1
Feb2
Bo [-]
Time [hr]